Volume 4
Number 2
February 2020
Pages 423–954

Sustainable Energy & Fuels

Interdisciplinary research for the development of sustainable energy technologies

rsc.li/sustainable-energy

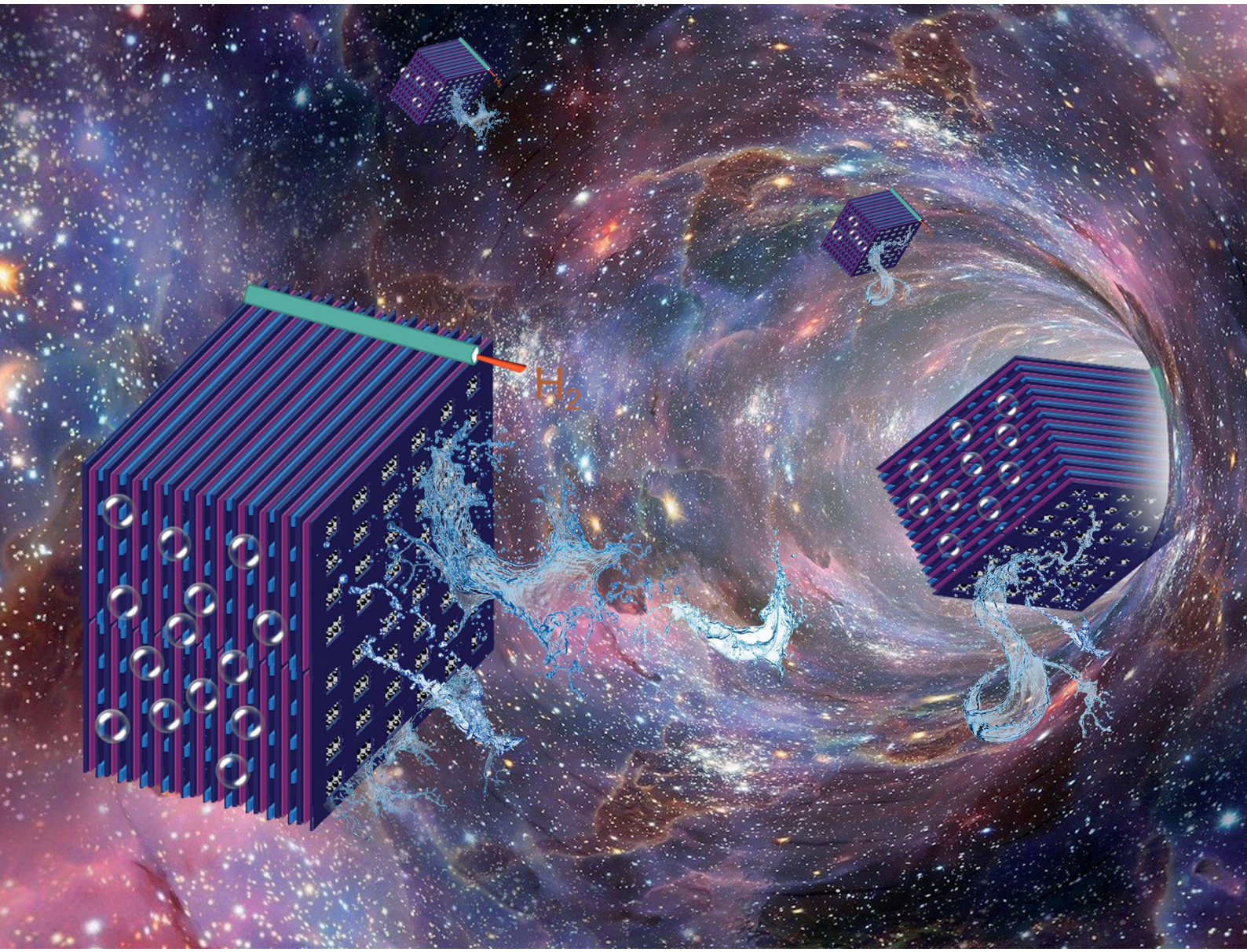

ISSN 2398-4902

ROYAL SOCIETY OF CHEMISTRY

REVIEW ARTICLE

Kondo-Francois Aguey-Zinsou *et al.*

Planar polymer electrolyte membrane fuel cells: powering portable devices from hydrogen

Sustainable Energy & Fuels

REVIEW

View Article Online
View Journal | View Issue

Cite this: *Sustainable Energy Fuels*, 2020, **4**, 439

Planar polymer electrolyte membrane fuel cells: powering portable devices from hydrogen

Prabal Sapkota,[a] Cyrille Boyer,[b] Rukmi Dutta,[c] Claudio Cazorla[d] and Kondo-Francois Aguey-Zinsou*[a]

Polymer Electrolyte Membrane Fuel Cells (PEMFC) are often viewed as enablers of decarbonised energy systems since they transform hydrogen directly into electricity with water as the main by-product. The attraction for fuel cells is also in their versatility because they can be implemented across a wide range of applications from microelectronics to large scale power generation. Herein, we review recent progress on the design and fabrication of PEMFC with a special focus on their air-breathing planar configuration as this extends the possibility of PEMFC to thin and flexible designs. To date, the deployment of planar PEMFC highly depends upon scientific progress and technological solutions for cost reduction and long-term durability including the development of better proton conducting membranes and platinum-free catalysts to drive the oxygen reduction and hydrogen oxidation reactions efficiently. Long term durability is another challenge that can be addressed through the advancement of inexpensive and lightweight current collectors and highly efficient gas diffusion electrodes for better distribution of the reactants while maintaining an optimum hydration of the proton conducting membrane. Innovative fabrication methods for the various components of planar PEMFC as well as effective stack design and assembly are also critical for efficiency maximization, reproducibility and overall cost reduction.

Received 26th September 2019
Accepted 15th November 2019

DOI: 10.1039/c9se00861f

rsc.li/sustainable-energy

[a]*MERLin, School of Chemical Engineering, The University of New South Wales, Sydney, NSW 2052, Australia. E-mail: f.aguey@unsw.edu.au*
[b]*CAMD, School of Chemical Engineering, The University of New South Wales, Sydney, NSW 2052, Australia*
[c]*School of Electrical Engineering and Telecommunications, The University of New South Wales, Sydney, NSW 2052, Australia*
[d]*School of Materials Science and Engineering, The University of New South Wales, Sydney, NSW 2052, Australia*

1. Introduction

The substitution of wood by coal has set the ground for the industrial revolution, but this is now leading to significant adverse impacts in terms of pollution. Renewable energy could enable a transition to new energy systems that may be more sustainable, but this requires advancing several technologies including better energy storage methods. Owing to its potential

Prabal Sapkota is currently a PhD candidate within the School of Chemical Engineering at the University of New South Wales under the supervision of Prof. Kondo-Francois Aguey-Zinsou and Prof. Cyrille Boyer. He obtained his MS in Energy and Power Conversion Engineering from Korea Institute of Science and Technology, South Korea. His research interest includes hydrogen energy and fuel cells.

Kondo-François Aguey-Zinsou completed a PhD in heterogeneous catalysis at the University Pierre et Marie Curie (Paris) in 2001. He carried-out post-doctoral research at The University of Queensland in bio-electrochemistry. He later moved to the research centre Helmholtz Zentrum Geesthacht in Germany, Queen Mary University London, and University College London where he supervised research projects on hydrogen storage, biofuel cells, and biomaterials. Since 2009, Francois is leading MERLin at UNSW. His research focuses on the development of advanced materials for hydrogen technologies.

to store energy with high density, hydrogen as a universal energy carrier could enable and support the uptake of renewables. Hydrogen can be generated *in situ via* decomposition of water, either by photocatalytic or electrical means.[1] Materials then can be used to reversibly store hydrogen safely with high density and efficiency.[2] Unlike electrochemical batteries, many hydrogen storage materials can be cycled for more than 20 000 times without any loss in storage capacity.[3] The stored hydrogen can then be converted back into electricity with fuel cells or combusted in engines. The advantage of fuel cells is in their ability to produce continuous energy as long as they are supplied with hydrogen.[4] Furthermore, the energy efficiency of fuel cells is constant even under varying loads.[5]

For small-scale applications, Polymer Electrolyte Membrane Fuel Cells (PEMFC) should have a high power density per volume and weight, be scalable to larger stacks and be of low cost across the main components, *i.e.* the catalysts, membranes and bipolar plates.[6,7] While large improvements have been made on each of these components as well as in terms of design, many challenges still exist. In particular, when considering small and portable applications, existing fuel cell stacks lack flexibility in their design, *i.e.* they are (i) not easily shaped into any form (the standard design is cylindrical or rectangle), (ii) still relatively heavy, and (iii) expensive. In particular, the cost of existing proton conducting membranes is still high and their durability low. There are also issues remaining in the replacement of platinum-based catalysts since the performance of current alternatives is not comparable.

With the increased digitalisation of our economy, there is a growing need for small fuel cells in terms of physical size for their integration into small and portable electronic devices,[4,8] including portable power.[9,10] In this respect, flat cells of a planar or cylindrical design are highly desirable.[11] Currently, planar designs have been found to be useful in applications where the power density per surface area is not an issue, in comparison to the overall thickens of the stack.[12] If well designed, planar PEMFC also provide silent operation, no parasitic load and this with a high current density.[9] Under a silent operation mode, the cathode side is opened for a self-breathing operation of the cell.[13]

Herein, recent progress in the design of planar PEMFC for portable/mobile applications is reviewed with the aim to summarise current state-of-art across fundamental research to advance the design of individual components and their assembly into functional devices. In particular, the general principles of fuel cells are reviewed as well as recent progress in the development of better catalysts and membranes. The design, working conditions and performance, as well as fabrication methods of existing planar PEMFC are reviewed. Based on current research progress, we foresee an imminent implementation and use of planar PEFMC in important industrial and commercial sectors, leading to more sustainable and environmentally respectful forms of energy consumption.

2. General principles of fuel cells

Fuel cells are electrochemical devices which convert chemical energy into electrical energy. The working principle of all fuel cells is the same and the basic structure is composed of an electrolyte, two electrodes (anode and cathode), and interconnects between the two electrodes and adjacent cells in the stack (Fig. 1).[5]

The overall chemical reaction taking place in PEMFC can be explained by considering the anode and cathode reactions. At the anode, the Hydrogen Oxidation Reaction (HOR) occurs with an activation energy of ~65 kJ mol^{-1} following reaction (1).[14]

$$H_2 = 2H^+ + 2e^- \ (E^\circ = 0\ V) \quad (1)$$

This activation barrier can be reduced with suitable catalysts such as Pt (18 kJ mol^{-1}).[15] When hydrogen reaches the Pt surface, dissociative adsorption of H_2 occurs,[16] followed by electron transfer from H_2 to Pt and finally the release of the adsorbed hydrogen takes place as shown in Fig. 2a. At the cathode (Fig. 2c and d), oxygen is reduced with an activation energy of 57.3 kJ mol^{-1} in presence of a catalyst, *e.g.* Pt,[15] according to the reaction:

$$O_2 + 4e^- + 4H^+ = 2H_2O \ (E^\circ = +1.228\ V) \quad (2)$$

The overall electrochemical reaction is thus expressed as:

$$2H_2 + O_2 = 2H_2O \ (E^\circ = +1.228\ V) \quad (3)$$

It is noteworthy that the activation energy for the recombination of O_2 with H^+ is high as compared to the energy required to split the H_2 molecule; and this is mainly due to the difficulty of breaking the strong double bond of molecular O_2 (activation energy: 498 kJ mol^{-1}).[17]

Ideally, the molecular Oxygen Reduction Reaction (ORR) involves 4 protons and 4 electrons. But a 2 electrons path is also possible depending on the activity of the catalyst (Fig. 2c and d).[15–22] During the electrochemical process, it is believed that O_2 is first adsorbed at the electrode surface where the breaking of the O–O bond leads to adsorbed oxygen atoms (2O*, Fig. 2b). These adsorbed atoms of oxygen can then react with a proton (H^+) to form a surface bounded OOH*. The surface bounded OOH* further reacts with H^+ and two electrons to form water, which then leaves the catalyst surface (Fig. 2d). In the alternative two-electron reduction pathway, O_2 does not undergo a dissociative chemisorption at the catalyst surface and is directly reduced to produce hydrogen peroxide (H_2O_2). H_2O_2 may further react at the catalyst surface or desorb (Fig. 2c). The formation of H_2O_2 is not desirable because H_2O_2 can lead to an oxidative degradation of the membrane.[23] The electrochemical reaction involving H_2O_2 also leads to a cell potential of 0.68 V, *i.e.* almost half the value of 1.228 V corresponding to the 4 electrons pathway. To avoid the formation of H_2O_2, the dissociative adsorption of O_2 at the surface of the catalyst into the adsorbed species *OOH should be facilitated (Fig. 2d).[19] Production of H_2O_2 is mainly occurring at the membrane/electrode interface due to reactants crossover and is found to increase at low humidity. At high humidity levels, the membrane channels are obstructed by the accumulated water molecules.[23] Catalyst like Au, carbon-based materials including

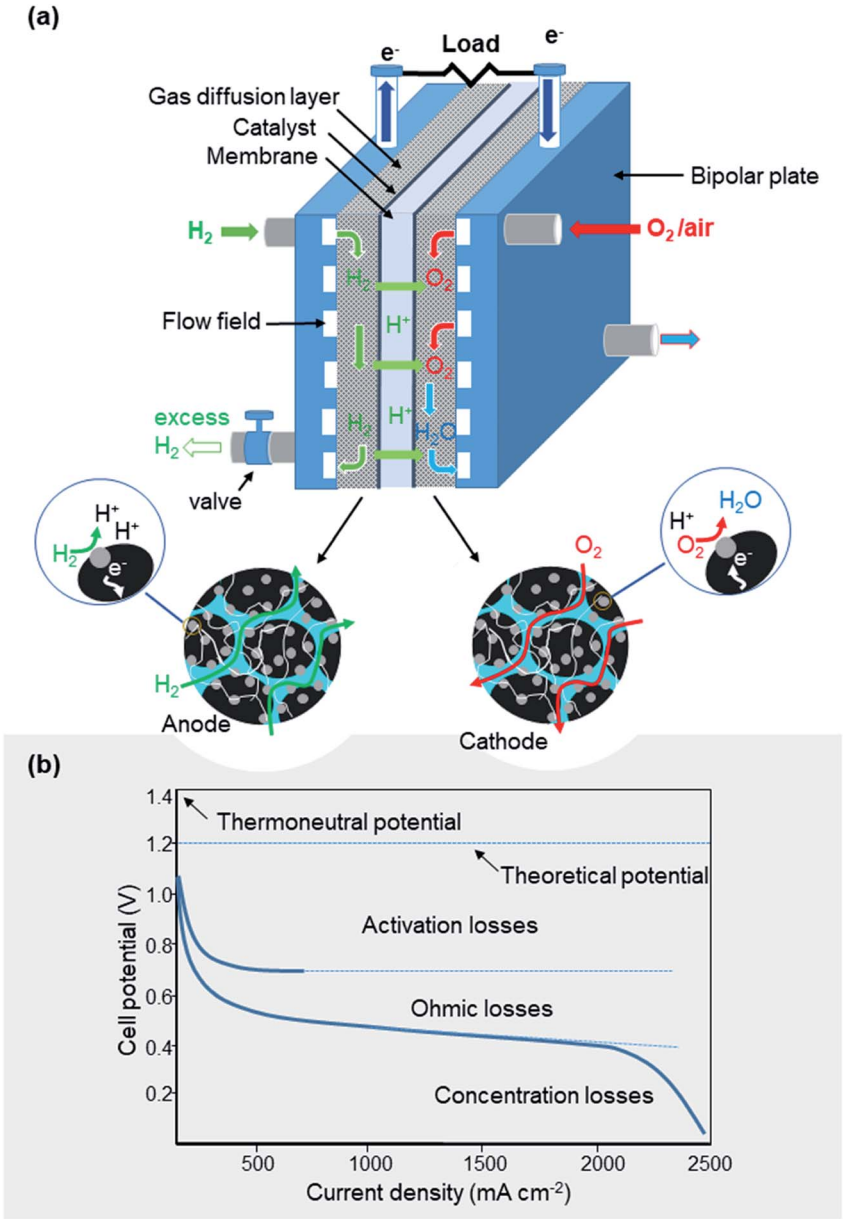

Fig. 1 (a) Schematic of a PEMFC where at the surface of the two electrodes the H_2/O_2 electrochemical reaction occurs. At the anode, the H_2 oxidation reaction (HOR) takes place and at the cathode, the O_2 reduction reaction (ORR) occurs, and (b) typical polarisation curve for PEMFC.

carbon nanotubes, and Pd–Hg alloys are found to be good at promoting the reduction of O_2 to H_2O_2 as a non-dissociative chemisorption of O_2 occurs at their surface due to the strong binding of OH* and OOH*.[19,24]

Under ideal conditions, the 4 electrons path dominates the 2 electrons path at a working potential above 0.3 V.[25–27] However, in the presence of catalyst surface impurities such as Al and Mo,[28] and at an electrode potential lower than ~0.8 V,[26] both the 4 and 2 electrons paths simultaneously occur. Several reasons have been proposed to explain this, including (i) the blockage of surface active sites by adsorbed hydrogen atoms preventing the dissociative adsorption of O_2,[29] (ii) the difficulty of forming bridge type adsorptions at different adjacent catalyst sites, which favours a Pauling (end on)[30] adsorption type and thus the H_2O_2 path (Fig. 2b),[16] (iii) the geometric arrangement of the atoms at the catalyst surface,[29] and (iv) the number of catalytic surface sites. Furthermore, at potentials higher than 0.8 V, adsorbed oxygen tends to be very stable (~237 kJ)[26,31] at Pt surfaces and this creates difficulties for the ORR to occur. The stability of oxygen can be reduced by lowering the potential; however, a minimum voltage of ~0.4 V is required to drive H_2O formation.[26,31,32]

In comparison to the cathode, the overpotential at the anode is lower because the exchange current density, *i.e.* the rate at which the chemical reaction proceed to equilibrium is much higher. Typically for Pt, this is in the order of 0.1 A cm^{-2} at the anode and 6 μA cm^{-2} at the cathode (*e.g.* with a PEMFC operated at 80 °C, with a H_2 and O_2 pressure of 1 bar and composed

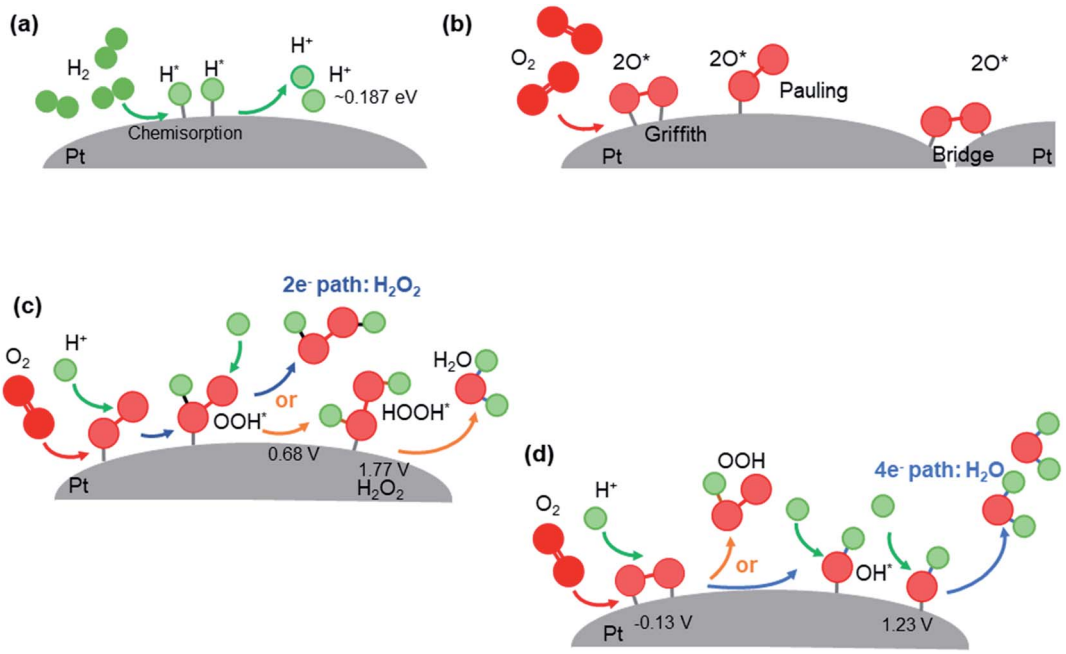

Fig. 2 Illustration of (a) H_2 oxidation reaction (HOR) mechanism at the surface of Pt, (b) mechanism of O_2 binding at the surface of Pt,[16] (c) possible pathways for O_2 reduction reaction (ORR) *via* a $2e^-$ mechanism at the surface of Pt, and (d) ORR *via* a $4e^-$ mechanism at the surface e of Pt. Values of 0.68, −0.13 and 1.23 V correspond to potential of the reaction *vs.* NHE.

of E-TEK (20% Pt/C) and Nafion 117).[15,33] This means that Pt is good for splitting H_2 but not so good for splitting O_2.[15] Additional overpotential at the electrodes may also be due to parasitic reactions that take place at the surface of the catalysts.[32,34] Apart from the formation of H_2O_2, formation of OH^- (reaction (4)), and radicals like OH^* and OOH^* as well as evolution of H_2 can also occur.

$$H^+ + O^- \rightarrow OH^- \ (E = 0.87\ V) \quad (4)$$

Furthermore, under a low H_2 concentration, the formation of CO_2 resulting from the reaction of water with the carbon substrate may also occur (reaction (5)). This not only reduces catalytic activity and the overall performance of the cell but also contributes to the corrosion of the carbon (C) electrodes.[35–37]

$$C + 2H_2O \rightarrow CO_2 + 4H^+ + 4e^- \ (E = 0.20\ V) \quad (5)$$

Understanding the thermodynamics involved in fuel cells is also important with respect to achieving an adequate energy balance, where the maximum work output (electric energy) obtained from the fuel cell (3) is equal to the free-energy change of the reaction (Gibbs free energy). In this case, the Gibbs free energy corresponds to the energy available to move the electrons in the external circuit. Hence, the Gibbs free energy change of the chemical reaction is related to the cell voltage as shown in eqn (6).[7]

$$\Delta G = -nFE \quad (6)$$

where ΔG is the free energy change, n is the number of moles of electrons involved, E is the reversible potential, and F is Faraday's constant. If there is no loss in the system or the reactants or products are in their standard states, the equation can be written as:

$$\Delta G^\circ = -nFE^\circ \quad (7)$$

For $n = 2$ and $F = 96\ 500$ C mol^{-1} electron at 25 °C, ΔG° is then equal to −237.13 kJ mol^{-1} of H_2O (liquid)[7] and from eqn (7), E° is determined to be 1.228 V. The negative value of ΔG° indicates that the process is exothermic and thermodynamically feasible.

Since the Gibbs free energy depends upon the temperature, pressure and concentration of the reactants, it can also be formulated along the Nernst equation as,

$$E = -\frac{\Delta G^\circ}{nF} + \left(\frac{RT}{2F}\right)\ln\left[\frac{P_{O_2}{}^{1/2}}{P_{H_2O}}\right] + \left(\frac{RT}{2F}\right)\ln(P_{H_2}) \quad (8)$$

where, E is equilibrium potential, P is the gas pressure, R is gas constant, and T is the absolute temperature. It can be inferred from (8) that higher potentials are reached by increasing the reactants activity at standard temperature (25 °C) and pressure (101.32 kPa).[7]

Furthermore, the enthalpy associated with the electrochemical reaction in PEMFC can be defined as the difference in heat formation (ΔH) between that of the products and reactants:

$$\Delta H = (h_f)_{H_2O} - (h_f)_{H_2} - (h_f)_{O_2} \quad (9)$$

Taking into account that the heat of formation of liquid water ($(h_f)_{H_2O}$) is −285.84 kJ mol^{-1} at 25 °C and the heat of formation of the elements is zero,[7] ΔH is −285.84 kJ mol^{-1}.

The negative value of ΔH indicates that energy is released, and this value can also be used to calculate the thermoneutral potential (E_t) of a PEMFC, *i.e.* the potential at which the fuel cell releases no heat.

$$\Delta H = -nFE_t \quad (10)$$

For a 4 electrons reaction path, E_t is then equal to 1.482 V, and this value corresponds to the voltage that can be generated if all the enthalpy of H_2 is converted to electricity. In reality, the maximum achievable voltage is 1.228 V (7), and thus the remaining energy is converted to heat as the process is exothermic.

H_2 is used in fuel cells to produce electricity, but it can also be burnt to produce heat. By considering both cases, the maximum efficiency of a fuel cell can then be calculated as,[7]

$$\eta = \frac{\text{electrical energy produced per mole of } H_2}{-\Delta H} \times 100\% \quad (11)$$

From (7), the maximum possible electricity generated is equal to Gibbs free energy, so (11) can be re-written as:

$$\eta = \frac{\Delta G^\circ}{\Delta H} \times 100\% \quad (12)$$

Hence, based on (12), the maximum efficiency of a fuel cell is 83%.

In practical systems, the operating efficiency is around 60% because of losses due to the cell design and side reactions (Fig. 1b). Potential losses include: (i) ohmic loss due to the internal resistance of the cell components, and (ii) concentration and activation gradients due to the inherent diffusion limitations of the reactants and products. Side reactions are linked to the selectivity of the catalysts and the effectiveness and permeability of the proton conductor membrane. By taking into account these losses, the cell voltage can be expressed as:

$$E_{cell} = E_{ocv} - \Delta E_{ohm} - \Delta E_{con} - \Delta E_{act} \quad (13)$$

where, E_{ocv} is the open circuit voltage of the cell, ΔE_{ohm} is the ohmic loss, ΔE_{con} is the concentration loss and ΔE_{act} is the activation loss as further expressed below.

The ohmic loss can be expressed as:

$$\Delta E_{ohm} = iR_{ohm} \quad (14)$$

where i is the operating current density and R_{ohm} is the area specific internal resistance ($\Omega\ cm^{-2}$) of the cell. R_{ohm} can be determined experimentally by the current interruption method,[38] and value typically ranging from 0.115–0.140 $\Omega\ cm^{-2}$ at temperatures <45 °C have been reported.[38] Improvement in cell design to facilitate the flow of gases and water, using membranes of high proton conductivity and high conductivity current collectors are all potential strategies to minimize ohmic loss.

On the other hand, concentration loss is due to a drop in concentration of the reactants at the electrode surface. Concentration loss can be determined by the current sweep method,[38] and formulated as:

$$\Delta E_{con} = m \exp(ni) \quad (15)$$

where m and n have constant values of about 3×10^{-5} V and, $8 \times 10^{-3}\ mA^{-1}$, respectively.

It is noteworthy that concentration loss is more prominent at high current densities when more reactants are needed. Accordingly, the main strategies to optimise this are through a careful design of the electrode structure, the reactants/products flow fields (flow channels) as well as by an increase in the pressure of the reactants, and/or the use of oxygen instead of air.

Activation loss is however, mainly due to the ORR at cathode because the reaction is often slow (*e.g.* turnover frequency $\sim 25e^-$ per site per s for Pt/C).[39] Activation loss can be determined experimentally by the current sweep methods and be expressed as:

$$\Delta E_{act} = A \ln\left(\frac{i}{i_o}\right) \quad (16)$$

where, A is a constant whose value is higher for slow chemical reactions, i_o is the exchange current density of a catalyst (typically in the range 10^{-2} to 10^{-4} A),[15] and i is the operating current density. The above equation is only valid for $i > i_o$.

To reduce the activation loss, it is important to increase i_o and this can be achieved: (i) by increasing the temperature and pressure of the PEMFC operation and the electrodes' surface area, and/or (ii) by using better catalysts.[38]

Taking this into account, several research directions have been investigated to improve the overall performance of PEMFC.[40] One area of focus has been on improving O_2 mass transfer at the cathode by using high surface area Ketjenblack carbon support and surface functionalisation for enhanced catalyst deposition, for example.[41] By using a polyol reduction process for Pt at the surface of Ketjenblack carbon an activity of $372 \pm 29\ A\ g^{-1}$ was reported at low catalyst loading (62–64 $\mu g\ cm^{-2}$).[41] Various Pt alloys have also been developed to increase activity while reducing Pt content.[42] Other areas of research have focused on developing better membranes to achieve higher proton conduction (*e.g.* sulfonated polyimide based membranes) under reduced humidity and/or at higher temperatures of operation.[43] These are further discussed below with a specific focus on planar fuel cells. Recent advances on other types of fuel cells have been described in additional excellent reviews[44,45] and books.[46]

3. Current state of the art in materials for planar PEMFC

Planar PEMFC correspond to a class of fuel cells with a minimised volume and mass as to reduce physical encumberment while achieving a higher power density. Hence, planar PEMFC have usually open air cathodes to allow passive, self-breathing operation without the need of cathode flow field and a fan for air/O_2 supply.[47] These fuel cells are also stripped to the maximum possible to reduce power consumption and parasitic

load. Their thin geometry is advantageous for applications in small and portable devices, but this also poses several challenges in terms of materials selection to achieve a maximum flexibility, minimum thickness, mechanical strength while effectively managing the flow of reactants and water.

Over the last decade, significant improvements have been made in terms of reduction in size and weight, enhancement in performance and ability to scale up planar PEMFC. Some of the examples include the development of high performing, light and flexible air breathing PEMFC (thickness 0.22 mm with a specific volume power density of 5190 W L^{-1}),[48] and better fabrication methods by thermal imprinting process and laser machined rollable ultra-light fuel cell stack delivering 508 mW for 10 cells with an energy density of 0.228 W g^{-1}, for example.[49] Hereafter, current progresses along these improvements are discussed for the different components of planar PEMFC.

3.1. Proton conductive membranes

Membranes are one of the key components of PEMFC. The membrane allows the free movement of H^+ ions from the anode to the cathode while ensuring insulation to avoid short-circuit. Materials suitable as membranes must meet key requirements including enhanced chemical resistance, mechanical strength and high proton conduction. Among the proton conducting materials explored to date, the most popular remains the Nafion (®Dupont) membrane invented in 1962.[7] However, the cost of this membrane remains high because of a complicated synthesis process (Fig. 3a),[50,51] involving dangerous reactions under high pressure and temperature, *e.g.* fluorination is an exothermic process that can become uncontrollable and ethylene is hazardous. In addition, the synthesis of the co-monomer commonly referred as perfluoro sulfonylfluoride ethyl propyl vinyl ether involves numerous steps with low yields.[40,52] Nafion is based on a sulphonated fluoroethylene backbone structure (Fig. 3a), and thus has the ability to enable proton conduction and water retention due to hydrophilic and hydrophobic moieties. The end of the side chain of the perfluorosulfonic polymer SO_3^- ion is highly hydrophilic and thus allows for high proton conduction (0.1 Ω^{-1} cm^{-1}),[7] while the polytetrafluoroethylene (PTFE) back bone structure provides

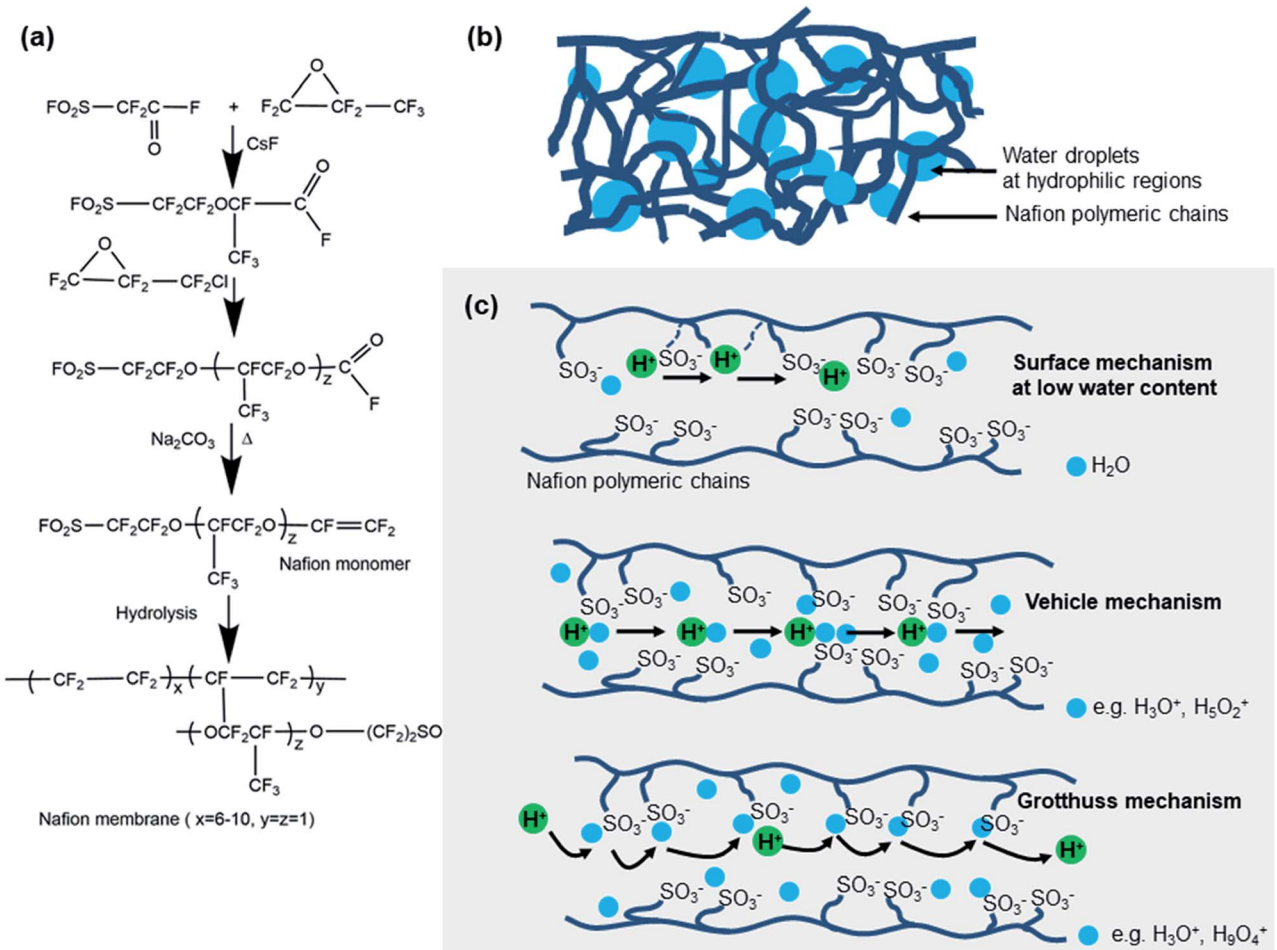

Fig. 3 (a) Nafion synthetic process.[50,55]. (b) Illustration of the macroscopic structure of hydrated Nafion-type membrane,[7,57] and (c) schematic representation of possible proton diffusion mechanisms in Nafion.[53,60,61] In the surface mechanism, protons jump from sites to sites along the polymeric chain. In the vehicular mechanism, at higher water levels, proton may diffuse through the membrane by forming various hydrogen–water ions. For well hydrated membranes, a Grotthuss mechanism can take place where the proton is transferred from one water molecules to the another one connecting the polymers side chains.

further resistance against chemical corrosion. The hydrophilic region around the sulfonic acid can lead to the absorption of large quantities of water (~20 molecules) for each SO_3^- side chain (Fig. 3b).[7] Hence, H^+ weakly coordinated to the SO_3^- groups can easily hop from sites to sites (Fig. 3c). Further diffusion between the separated hydrated regions occurs following a vehicular diffusion mechanism through connecting water pathways (Fig. 3c).[53–61]

Proton transport in Nafion is usually described along three mechanisms: surface diffusion, Grotthuss hopping and vehicular diffusion (Fig. 3c).[53] The surface diffusion mechanism occurs close to the pore wall (~1 nm from the pore wall) or under low water content (<5 water molecules per sulfonic acid group).[53,59] In this case, protons hop between adjacent sulfonic acid sites. At higher hydration levels (>5 water molecules per SO_3^-), both Grotthus and vehicular mechanism are found to occur.[59] In the Grotthus mechanism, protons hop from one hydrolysed ionic site (SO_3^- H_3O^+) to another across the membrane (Fig. 3c) and this mechanism is dominant at hydration levels corresponding to 5 to 10 water molecules per sulfonic acid group. Protons hopping can also occur across the Zundel cation ($H_5O_2^+$) at low water content or across the Eigen cation ($H_9O_4^+$) at higher hydration levels. In contrast, in the vehicular mechanism, the hydrated proton (H_3O^+) diffuses through the aqueous membrane by electro-osmotic flow (Fig. 3c).[55,56]

The activation energy (E_a) for protons hopping drops quickly as the number of water molecules available at the SO_3^- sites increases (*e.g.* E_a ~0.35 and ~0.1 eV for 3 and 10 water molecules per SO_3^-, respectively). Similarly, the proton diffusion coefficient increases at increased levels of hydration (for example 0.014×10^{-4} and 0.17×10^{-4} cm^2 s^{-1} for 6 and 15 water molecules per SO_3^-, respectively at 25 °C).[59] At higher hydration levels, both hopping and vehicular mechanisms have diffusion coefficients of 7×10^{-5} cm^2 s^{-1} and 1.71×10^{-5} cm^2 s^{-1} suitable for proton transport, respectively. Usually the mean hopping step time for H^+ surface diffusion is higher (1.61×10^{-9} s) than that for the Grotthuss (1.5×10^{-12} s) and vehicular (5.75×10^{-12} s) mechanism. This is due to the larger distance between the ionic groups (SO_3^-) at the membrane surface and thus the lower diffusion coefficient (~1.01×10^{-7} cm^2 s^{-1} at 25 °C) at the surface.[53,54,59] Such a behaviour further reduces water accumulation near the surface due to hydrophobic nature of the PTFE back bone.[62]

Although the most popular PEMFC membranes are based on the Nafion structure and thus hydrated perfluorosulfonic polymers, there are issues related to the use of sulfonic polymers. In particular, perfluorosulfonic membranes require a high humidification (~100%) to achieve ionic conductivity of 0.1 S cm^{-1}, and this poses problems when the fuel cell is operated at >80 °C, because water is partially vaporized. Perfluorosulfonic polymers have a limited operation temperature range of 0 and 100 °C, while an operation temperature of fuel cells at ~160 °C is preferable to minimise the activation loss and increase catalysis activity. Furthermore, membranes based on perfluorosulfonic suffer from permeability issues in the form of water and reactants cross-over because of the existing porous hydrophilic domains.[63] Hydrogen cross-over current densities of 0.12 mA cm^{-2} are typical for Nafion 117 at 60 °C.[64]

For the large scale deployment of fuel cells, alternative membranes with superior performance and lower cost of manufacturing are highly desirable.[65] Several alternative membranes have been researched and these are summarised in Table 1.[66–77] The strategies that have been explored for the development of new solid state electrolytes have focussed on cost reduction, higher temperature operation (≥160 °C), improved water uptake capacity and enhanced proton conductivity and stability. Membranes based on low cost aromatic polymers[74,78–81] including sulfochlorinated polyethersulfone, sulfonated poly(benzoxazole thioether sulfones) and vinylidenefluoride have been shown to display a good conductivity of ~0.235 Ω^{-1} cm^{-1} at 92 °C and a lower activation energy of 6–9 kJ mol^{-1} in comparison to Nafion 212 (9 kJ mol^{-1}).[74] These membranes also display a better water uptake capacity of 47–58 wt% at 25 °C (Nafion, 32 wt%) due to their higher degree of sulfonation. Furthermore, membranes with bifunctional sulfonic acid (–SO_3H) and carboxylic acid (–COOH) groups showed improved conductivity (~0.124 Ω^{-1} cm^{-1} at 25 °C) and water uptake (~32 wt% at 25 °C) mainly due to availability of a larger number of sulfonic and carboxylic function groups.[82]

The concept of hybrid (organic and inorganic composites) membranes has also been largely investigated owing to the potential of achieving better mechanical and thermal stability (up to 300 °C) with better water retention upon the addition of an inorganic phase.[83–88] For example, a membrane based on phosphonic acid polymers, grafted onto functionalized silica nanoparticles, and then dispersed in a matrix of poly(-vinylidenefluoride-*co*-hexafluoropropylene) displayed 800 mW cm^{-2} at a current density of 1.5 A cm^{-2}. For such a composite membrane, the water uptake of the membrane was 56–71 wt% and thermal stability of ~300 °C.[83] The possibility of making fluorine free membranes has also been investigated because of the higher versatility in molecular design and synthesis, and thus the possibility of achieving lower cost.[84,85] In particular, a polyphenylene-based membrane reached a proton conductivity of 0.22 Ω^{-1} cm^{-1} at a relative humidity of 95% with a water uptake 2.2 to 2.8 times that of Nafion.[85] Similarly, a sulfonated benzophenone membrane was reported to achieve a proton conductivity of ~4×10^{-2} S cm^{-1} at low humidity (20% at 80 °C).[84] This was explained by the better separation of hydrophilic-hydrophobic domains.[84] The composite membrane based on sulfonated poly(arylene ether sulfone) (SPAES) and perfluorosulfonic acid (PFSA) with a water uptake capacity of 56–66 wt% also displayed a conductivity of 0.1–0.2 Ω^{-1} cm^{-1} at 80 °C and improved mechanical strength.[88] Additional details can be found in recent reviews on membranes for PEMFC.[43,89] It is noteworthy that from current developments no commercial viable product has emerged and thus to date Nafion still remains the first choice.

3.2. Catalysts for ORR and HOR

A key issue that also needs to be resolved for the large scale commercialization of fuel cells is the development of non-

Table 1 Summary of properties of selected membranes for proton conduction

Membrane types		Operating conditions: temperature, relative humidity	Performance	References
Perfluorinated	Perfluorosulfonic (Nafion)	0–100 °C, 100%	Conductivity: 0.1–0.2 Ω^{-1} cm^{-1} Operating hours: ~60 000 h Power density: 400–1200 W cm^{-2} Electrochemical stability: very good	66, 68 and 69
	Perfluorosulfonic (Aciplex)	~80 °C, 100%	Conductivity: 0.11 Ω^{-1} cm^{-1} Operating hours: < 60 000 h Power density: 750 mW cm^{-2} Electrochemical stability: good	68
	Perfluorosulfonic (Flemion)	~80 °C, 100%	Conductivity: 0.14 Ω^{-1} cm^{-1} Operating hours < 60 000 h Power density: 450–700 mW cm^{-2} Electrochemical stability: good	68
	Perfluorosulfonic Fumapem®	~25 °C, 100%	Conductivity: ~0.058–0.1 Ω^{-1} cm^{-1} (from Fumatech technical specifications)	67 and 70
	Gore select™	~25–80 °C, ≤ 100%	Conductivity: 0.063 Ω^{-1} cm^{-1} Operating hours: >3000	69 and 71
	Perfluorocarboxylic acid	100%	Conductivity: 0.023 Ω^{-1} cm^{-1}	66 and 72
Partially fluorinated	TFS (α,β,β-trifluorostyrene) BAM3G	~80 °C	Conductivity: 0.05–0.9 Ω^{-1} cm^{-1} Operating hours >15 000	43 and 73
	Styrene grafted and sulfonated poly(vinylidenefluoride) [PVDF-*g*-PSSA]	~60 °C	Conductivity: 0.027 to 0.24 Ω^{-1} cm^{-1}	66 and 74
Non fluorinated	Sulfonated polyimide	40–100 °C	Conductivity: 0.002–0.04 Ω^{-1} cm^{-1} (first generation) 1.67 Ω^{-1} cm^{-1} (next generation)	43 and 66
	Sulfonated poly(4-phenoxy benzoyl-1,4-phenylene) [S-PPBP]	60–160 °C, 100%	Conductivity: 0.02 Ω^{-1} cm^{-1} Power density: 300 mW cm^{-2}	66 and 75
	Sulfonated polybenzimidazoles [S-PBI]	60–160 °C, 100%	Conductivity: 0.03 Ω^{-1} cm^{-1} Power density: 200 mW cm^{-2}	43 and 66
	Sulfonated-poly (*p*-phenyleneterepht halamide) [S-PPTA]	26–90 °C, 100%	Conductivity 0.001–0.01 Ω^{-1} cm^{-1} Current density: 0.4–0.58 A cm^{-2} Operating hours: 230–500 h	43 and 66
	Imidazole doped sulfonated polyether ketone [S-PEEK]	80–130 °C, 100%	Conductivity: 0.03–0.11 Ω^{-1} cm^{-1} Operating hours: 3000–4000 h Power density: 325–350 W cm^{-2} Electrochemical stability: good	43 and 66
Others	Poly(2-acrylamido-2-methylpropane sulfonic acid) [poly-AMPS]	30–90 °C, 30–80%	Conductivity: 0.038 Ω^{-1} cm^{-1} Electrochemical stability: good	66 and 76

Table 1 (*Contd.*)

Membrane types		Operating conditions: temperature, relative humidity	Performance	References
	Supported composite membrane (sulfonated poly(ether ether ketone)/ polydopamine modified graphene oxide) [SPEEK/ DGO]	30–120 °C, 0–100%	Conductivity: 0.003 Ω^{-1} cm^{-1} (anhydrous condition) 0.2 Ω^{-1} cm^{-1} (hydrous condition)	66 and 77
	Current density: 698 mA cm^{-2}			
	Polybenzimidazoles (PBI) Fumapem®	~170 °C	Conductivity: 0.07–0.09 Ω^{-1} cm^{-1}	67 and 68
	Hybrid (organic–inorganic), phosphonic acid grafted silica nanoparticles and poly(vinylidenefluoride-*co*-hexafluoropropylene)	20–140 °C, 0–100%	Conductivity: 0.053 Ω^{-1} cm^{-1} (80 °C) Current density: 1.5 A cm^{-2} at 60 °C	83
Thermal stability: >300 °C				

noble, low-cost and effective catalysts of high turnover frequency and selectivity, and resistance to poisoning.[90] To date, Pt supported on carbon has remained the most widely used catalyst for the HOR and ORR.[9,12,13] The amount of Pt loading can vary depending on the desired fuel cell performance but typically the Pt loading is around 0.3–0.4 mg cm^{-2},[91–93] and this leads to a power output of ~0.41 A cm^{-2} at 0.5 V. The best balance between PEMFC performance and durability is believed to be at 20 wt% Pt loading with 25% carbon black in the support layer. However, the highest ORR mass activity (~25 mA mg^{-1}) was obtained at 75% carbon black content in the support layer.[94] Addition of carbon black improved ORR mass activity and electrical conductivity.[94]

The issues of high cost (~50% of the total stack cost) and scarcity of Pt are significant (Fig. 4a).[95] One feasible solution is to reduce the amount of Pt loading on both the electrodes and this has been done *via* two approaches: (i) optimization of electrode structures to increase the number of active sites per gram of catalyst loading, or (ii) by alloying Pt with other elements.[96] For example, by alloying Pt with metals such as Fe, Co, Ni, Cu, and Cr; and/or by controlling atomic arrangement in the nanocatalyst (*e.g.* core–shell, optimized morphology/ facets, and ordered intermetallic structures), the electronic structure the catalytic active sites can be adjusted to the required levels while using less Pt.[97–99] The ultimate solution is however to fully replace Pt by non-noble and abundant elements. Fig. 4 summarises the current state of art in the search of alternatives to Pt and/or partial substitution of Pt. The various catalysts for the HOR and OOR can be classified in six broad categories: Pt/C (where C is carbon), Pt and Pt alloyed/de-alloyed structures, core–shells, non-precious metal catalysts, shape-controlled nanocrystals and nanoframes[100] as further discussed below.

The catalyst requirement for both conventional PEMFC (air/ oxygen supplied from external sources) and planar (self-breathing) PEMFC are the same. However, the amount of loading at the cathode must be higher because of the slow ORR.[29] Table 2 summarises different types of catalysts, their cost and performance at given loadings.[101–110] The target set by the US DOE is a loading of 0.125 mg cm^{-2}.[111,112] Current catalyst loading is much higher and in the range of 0.1 and 0.5 mg cm^{-2}.[29] Catalysts based on conductive polymers such as polypyrrole can be produced at a lower cost, but the performance is low (0.12 A cm^{-2} at 0.4 V)[113] in comparison to Pt/C (~0.41 A cm^{-2} at 0.5 V).[91–93]

3.2.1. Pt based catalysts for ORR. In early 1990s, several Pt alloys including those based on PtNi, PtCo and PtCr have been explored and higher activities were found in comparison to Pt/ C,[114–116] with a 2–3 fold increment in activity (Fig. 4b).[95] The enhanced activity was explained by the fact that non-precious metal bonds oxygen more weakly with an energy of 0.0 to 0.4 eV compared to the ~2.4 eV of Pt.[114] For example, it was observed that the current density of ORR on Pt_1Pd_1/C was 1.7 times greater than the commercial Pt/C (0.567 mA cm^{-2}) at 0.85 V.[117] Pt–Pd/C had comparable performance and better durability than the conventional Pt/C.[116]

A new approach to prepare Pt_3Co intermetallic nanoparticles through a facile thermal treatment of Pt nanoparticles supported on Co doped Metal Organic Framework (MOF) was also proposed. The obtained Pt_3Co nanoparticles achieved a significantly enhanced activity and stability owing to both improvements in electronic and mechanical property with the MOF support.[97] Similarly, PtNi alloy ($Pt_{0.61}Ni$/C) with a low amount of Pt (2.76 wt%) achieved power density of 1.1 W cm^{-2}.[118]

The use of a core–shell approach in catalysts design was also investigated with the aim to alter the electronic properties of the active catalytic sites, improve structural stability, and thus the overall catalytic activity.[119] Core–shell can be synthesised through various approaches including first the growth of a core and then a shell, one-pot synthesis, and de-alloying

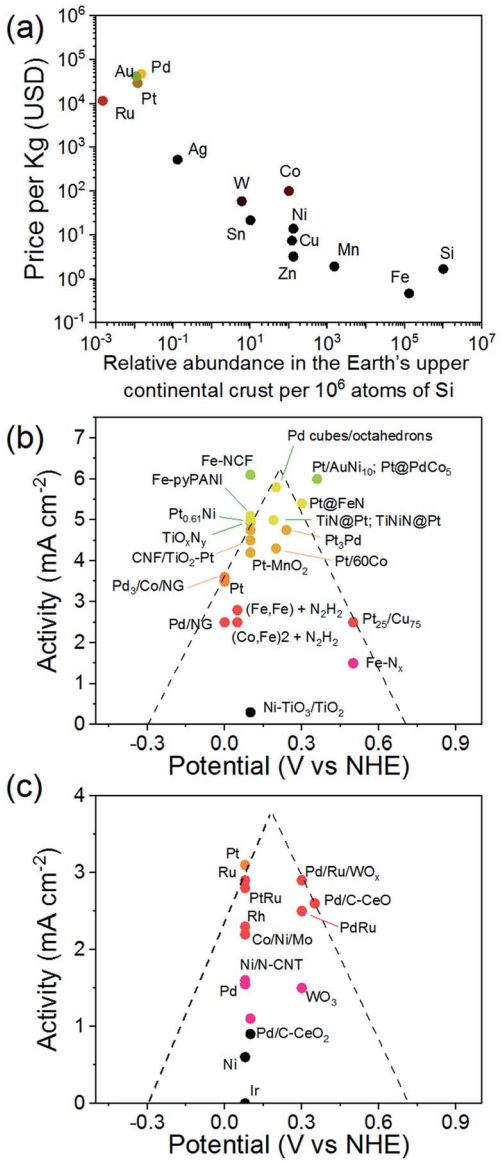

Fig. 4 (a) Price of elements (taken from Shanghai Metals Market, 07 Dec 2018) at the basis of potential catalyst for PEMFC as a function of their relative abundance in the Earth crust,[95] (b) volcano plot illustrating the potential of selected catalysts for O_2 reduction reaction (ORR), (c) volcano plot illustrating the potential of selected catalysts for H_2 oxidation reaction (HOR).

methods.[120,121] For example, for a core–shell catalyst (TiNiN@Pt) prepared by placing several layers of Pt atoms on the surface of nanoparticles of titanium nickel binary nitride (TiNiN), displayed an increase in activity of 200% in comparison to commercial Pt/C.[122] Possible reasons for such a good performance are the high dispersion and utilization of Pt, Ni doping, good stability of the nitride support, and a strong interaction between Pt and the TiNiN support. As a general rule, the addition of Ni, Co or Fe in Pt alloys increases the ORR activity and the addition of nitrogen in the core further increases the activity in the order of PtNiN/C > PtFeN/C > PtCoN/C.[123] De-alloyed core–shell nanostructures have also been synthesized.[124] In the case of PtCu, de-alloying of Cu surface atoms from Cu-rich Pt–Cu alloy precursors was done by electrochemical dissolution. The de-alloyed catalyst consisted of a core–shell structure made of a multilayer Pt rich shell surrounded by a Pt-poor particle core.[124] Similarly, a core–shell with a Pt monolayer on top of either Ir or Pd_3Co/C displayed a good mass activity of 1.01 A mg^{-1} and 0.57 A mg^{-1} for the ORR, respectively. These activities are greater than the US DOE target of 0.44 A mg^{-1}.[125] Fig. 4b summarises current findings along several catalysts reported so far.

By controlling the shape of the catalyst, it is expected that specific surface planes with appropriate binding energies to O_2 will be preferably exposed and stabilised. For example, branched Pd–Pt nanodendrites with highly exposed facet ratio {111} to {100} and unsupported Pt and PtPd nanotubes showed enhanced ORR and stability than Pt/C.[125–127] Lee *et. al.* reviewed various Pt nano-architectured catalysts for ORR in low temperature PEMFC and reported that the performance of Pt_3Ni_1 nanoframes with {111} facets was very high (5.7 A mg^{-1}).[128,129] This was explained to result from a downshift of the d-band centre of pure Pt upon Ni addition, and thus a resulting activity of Pt_3Ni_1 {111} facets10 times higher than the activity of Pt {111} and 90 times that of commercial Pt/C.[128] In the Pt based polyhedron catalysts including nanocaged PtNi/C, nanoframed Pt_3Ni/C, octahedral Pt_1Ni_1/C and cuboctahedral Pt/C, the addition of Ni also led to better current density in the range of 300 to 430 mA cm^{-2}.[130] In comparison, a current density of 20 mA cm^{-2} was reported from carbon supported cuboctahedral Pt.[131] In this case, it was claimed that Ni enables to bind O_2 more weakly than pure Pt.[130]

In addition, the surface structuration of catalyst nanoparticles provides a means to tune the catalytic activity, in particular for ORR, where several adsorption intermediates exists.[132] The interaction energy between the catalyst surface and these intermediates depends on the metal used as a catalyst and its surface structure. For example for Pt, the specific activity is found to be in the order of 1.77, 1.40 and 0.28 mA cm^{-2} for Pt {720}, Pt {111} and Pt {100}, respectively.[133] Hence, O_2 adsorption is favoured on {720} facets.[133,134] However, the activity of Pt has been found to be better enhanced by alloying Ni. In this case, the calculated activation energy related to the ORR as function of specific surface please evolves as follows: Pt (100) 0.80 eV > Pt/Ni (100) 0.79 eV = Pt (111) 0.79 eV > Pt/Ni (111) 0.15 eV.[134,135]

3.2.2. Non-Pt based catalysts for ORR. Although a noble metal, the use of Pd for the HOR and ORR in PEMFC has been widely investigated because it is more abundant than Pt (Fig. 4a).[115] ORR at Pd is of a slightly lower activity (0.024 mA cm^{-2} at 0.9 V)[136] compared to that of Pt (~1.2 mA cm^{-2} at 0.9 V) but with the addition of suitable metals like Co, Ni and Fe the activity of the resulting Pd alloys is similar to that of Pt (Fig. 4b).[137,138] For example, Pd_2Co showed a catalytic activity similar to that of commercial Pt (~0.8 mA at 0.8 V).[138] By controlling the shape of Pd nanocrystals to expose specific surface sites, *e.g.* {100}, the activity of Pd/C cubes was higher than that of commercial Pt/C for the ORR.[139]

Table 2 Comparison of typical catalysts for ORR. US Department of Energy (US DOE) targets for vehicles with the assumption that similar target would apply to portable electronic. The price of the catalyst was estimated from current chemical prices at the gram scale

Catalysts	Loading (mg cm^{-2})	Activity (mA cm^{-2})	Cost ($ per mg)	Cost ($ per cm)	References
US DOE 2020 targets	0.125			~0.023	101, 102, 111 and 112
Platinum					
Pt black	25	—	0.212	5.3	101
20% Pt/C	1	160	0.082	0.082	102
40% Pt/Ketjenblack	0.6	1000	0.143	0.085	103
Platinum alloy					
30% Pt_3Co	0.2	500	0.278	0.56	104
15.2% PtCo/C	0.005	2000	0.270	0.014	306
Core shell					
20% Pt–Cu/Vu core–shell nanoparticle catalyst	0.169	2500	0.278	0.56	105
Pt_3Co	0.033	3500	0.270	0.014	106
Shape controlled nano-crystals					
20 nm Pt multi-octahedrons	0.015	0.8	0.185	2.77×10^{-6}	101 and 107
Non-precious metals					
Conductive polymers Co-PPy/C	Ratio of C : PPy : Co = 0.7 : 0.16 : 0.13, cathode loading: 0.35	120	0.052	0.004	108–110 and 113

Even though the ORR turnover frequency of non-precious metal catalysts, *e.g.* Fe/PTCDA (perylenetetracarboxylic dianhydride) is generally lower (~1.7e^- per site per s)[96] than that of Pt (25e^- per site per s),[96] such catalysts could be an acceptable solution as the cost of Pt is high. In this regard, transition metal–nitrogen–carbon complexes have been considered as promising candidates to replace Pt,[140–151] because of their relatively good performance (0.91 W cm^{-2}), good stability,[140,152] and better tolerance to CO than Pt.[141] For example, strong catalytic activity of Fe–N_x/C towards ORR has been reported with overall electron transfer number of 3.6, which is close to the theoretical 4 electrons ORR path (Fig. 2d).[142] A peak power of 570 mW cm^{-2} for a PEMFC with Fe/N/C as a catalyst was also reported.[146] Tungsten carbide (WC) nanoparticles have also been reported to lead to reasonable fuel cell performances and membrane stability owing to the strong binding of OH^* (~2.29 eV) and H^* (0.63 eV) on WC.[150]

ORR catalysts based on heteroatoms doped carbon nanomaterials, *e.g.* nitrogen doped carbon nanotubes and graphene, boron doped graphene, and sulphur doped graphene[153] have also been investigated due to their high catalytic activity, better tolerance to fuel cross-over, low cost and better durability.[151,154] Recently, metal porphyrins and phthalocyanines with nitrogen and Co/Fe precursors have been reported to display good catalytic properties. In particular, composite catalysts like C–Co–N showed high ORR activity and good durability.[155] The cobalt–polypyrrole composite also gave a power density of 0.15 W cm^{-2} and a stable catalytic activity over 100 h.[155] Pyrolysis of spherical polyimide nanoparticles with Fe led to a catalyst that delivered 1.0 A cm^{-2} at 0.46 V at 80 °C.[156] This catalyst had a reasonable durability of 600 h. Furthermore, a catalyst prepared by electrospinning a polymer solution of ferrous organometallics and zeolitic imidazolate framework followed by thermal activation delivered a volumetric activity of 3.3 A cm^{-3} at 0.9 V.[157] Multi-step pyrolysis of polyimide (100 nm diameter) was also reported to provide a current density of 1.0 A cm^{-2} at 0.6 V.[158] Additional in depth advances on OOR catalyst can be found in recent reviews.[159,160]

3.2.3. Catalysts for HOR. Significantly less work has been done on the anode catalyst for HOR, and one of the reasons may be the lower amount of Pt needed at the anode because at this electrode the reaction is fast in comparison to ORR. The activity of various catalysts for HOR is summarised on Fig. 4c.[20,161–164] Among these various catalysts, Pt remains the most popular. However, other catalysts including Pd, Co, Ir and Ru in the form of bimetallic catalysts such as Pd_3Co, IrRu and Pd_xIr_y have also been explored.[165–168]

Pd-rich–Pt alloy (5% Pt) have been reported to have similar performances to that of Pt for HOR due to the so claimed synergetic effect between Pt and Pd.[139,169] Pd_3Co supported on partially exfoliated carbon nanotubes was used as a catalyst for PEMFC and a power density of 327 mW cm^{-2} at 60 °C was obtained. This corresponds to 65% of the power density reached with commercial Pt/C.[170] Similarly, when PdRu or PdIr was coupled with WO_x as the anode, the cell performance was reported to be enhanced.[171] In this case, WO_x acted as a hydrogen storage medium through the formation of a hydrogen tungsten bronze phase leading to the improvement of HOR at the Pd

surface. Further, Fe-based catalysts showed strong Fe–H reversibility during H* adsorption/desorption and these catalysts led to a high current density of 600 mA cm^{-2} at 0.4 V and a good stability.[172]

Apart from Pt and Pd, Ni has also been considered as potential candidates for HOR. Ni_3N supported on carbon was reported to lead to the highest mass activity (24.38 mA mg^{-1}) among the non-platinum based catalysts.[173] The enhanced performance is due to a downshift of the Ni d-band upon the formation of Ni_3N and interfacial charge transfer from Ni_3N to the carbon support leading to a weak binding of hydrogen on Ni_3N/C.[173] In case of HOR, edges/vertices have been shown to be more catalytically active.[174] The H_2 adsorption and desorption region in polycrystalline Pt is believed to be a union of Pt {110}, Pt {111} and Pt {100} facets.[174,175] Future research direction should thus focus on the synthesis and stabilisation of particles with a maximum of highly active edges/vertices as this could enable lower amounts of Pt (~μg cm^{-2}) while retaining a high current density.[174] Additional recent work on HOR catalysts is summarised in excellent reviews.[176]

3.2.4. Alternatives to carbon as a catalyst support. Carbon based materials have been widely used as supports for Pt based catalysts. However, problems including carbon oxidation, catalyst sintering or agglomeration have been reported when carbon is used as a catalyst support.[177] In order to address these issues, alternative support materials such as metal oxides (*e.g.* titanium dioxide, iridium oxide, tungsten oxide and tin oxides), metal nitrides (*e.g.* titanium nitride), carbides (*e.g.* boron carbide, titanium carbide, silicon carbide, tungsten carbide) has been investigated.[153,177] For example, the performance of Pt supported on Ti_4O_7 was reported to be close to commercial that of Pt/C.[148] Furthermore, Pt supported on C–MnO_2 also exhibited better activity (1.6 A cm^{-2} at 0.529 V) and stability than Pt/C (1.6 A cm^{-2} at 0.209 V).[149] An oxide-carbon nanofibrous composite support was also used to develop carbon nanofibers/TiO_2–Pt nanofibrous catalysts. These displayed a high ORR activity (995 mW cm^{-2}),[178] and the improvement observed was explained as a result of the strong metal support interaction.

3.3. Gas diffusion layer

The Gas Diffusion Layer (GDL) usually sits on top of catalyst layer coated at the surface of the proton conducting membrane and thus acts as a current collector (Fig. 1a). The assembly of two GDLs, one of each side of the catalyst coated membrane, forms the Membrane Electrode Assembly (MEA). The GDL facilitates supply of the reactants (H_2 and O_2) to the catalyst layer. The GDL also permits the transport of the by-product (water) outside the cell, and provides mechanical strength to individual cells.[179,180] The basic structure of the GDL consists of a macroporous substrate on which microporosity is added in the form of a catalyst ink. The macroporous substrate is usually a carbon paper (*e.g.* Toray carbon paper, 0.15–0.25 mm thickness, and ~75% porosity)[181,182] or cloth which acts as a gas distributor and current collector. The microporous layer is usually made from Pt/C powder (*e.g.* Vulcan XC-72R), a binder (Nafion solution) and a hydrophobic agent (PTFE, 30–60 wt%).[181–185] This mixture is then coated, *e.g.* by screen printing with a loading density of 1.5 mg cm^{-2},[183] on the side of the macroporous substrate in contact with the proton conducting membrane.[181,182]

It is essential for the GDL to maintain both hydrophobicity and hydrophilicity as it needs to transport humidified reactant gases to the catalytic layers and transport water (as a vapour or liquid) outside the catalytic layer.[182,184] If the water accumulates in the GDL, the porosity is blocked, and the power output of the cell is reduced because the reactants cannot reach the catalyst/membrane interface. Controlling this amount of residual water is particularly important at the cathode where water is formed.[181]

Typical GDLs have a porosity of 40 to 60%, a thickness of ~300 μm, and a PTFE content of ~20 wt%.[185] PTFE is commonly used as a hydrophobic agent in GDLs to facilitate the removal of water as a by-product of the electrochemical reaction. However, excessive PTFE amounts can lead to an increase in mass transfer resistance because of the reduced available porosity.[184] To develop an effective GDL, it is thus important to understand the multiphase and dynamic in water uptake and removal for the GDL. Such an understanding can be framed by taking into account the capillary and viscous forces involved and these can be defined in terms of dimensionless capillary number (C_a) and viscosity ratio (M):[186,187]

$$C_a = \frac{u\mu_{nw}}{\gamma} \tag{17}$$

$$M = \frac{\mu_{nw}}{\mu_{wet}} \tag{18}$$

where u is the superficial viscosity of non-wetting phase, γ is surface tension of water, μ_{wet} is the wetting and μ_{nw} is non-wetting phase viscosities of GDL.

Under normal PEMFC operation, C_a is in the range of 10^{-8} to 10^{-5} and M is ~17.5 and water flows out of the GDL through a capillary fingering regime.[186] Outside these conditions, other regimes exist. For $M \sim 1.5 \times 10^{-2}$ and $C_a \sim$ in the range of 10^{-5} water forms multiple fingers like shape and this leads to a viscous fingering regime. Finally for $M \sim 64$ and $C_a \sim$ in the range of 10^{-3} to 10^{-4}, a stable displacement regime where water is evenly distributed in GDL is established.[186–188]

Removal of liquid water from the fuel cell should overcome two main barriers: the breakthrough pressure and the droplet adhesion force ($F_{adhesion}$). Breakthrough pressure corresponds to the maximum capillary pressure (P_c) that must be overcome by liquid water to flow outside the GDL and is calculated as:[186,188,189]

$$P_C = P_L - P_G = \frac{-2\gamma\cos(\theta)}{r} \tag{19}$$

where θ is the contact angle of the water/air/GDL interface, r is the radius of the pore in the GDL, P_L is the liquid phase pressure and P_G is the gas phase pressure.

The droplet adhesion force ($F_{adhesion}$) corresponds to the force a water droplet needs to overcome to move along the GDL's surface and this is determined as:[190]

$$F_{\text{adhesion}} = \frac{\rho V g \sin \theta_s}{\Pi d_w} \quad (20)$$

where ρ is the water density, V is the droplet volume, g is gravitational constant, θ_s is the sliding angle (*i.e.* the angle at which a water droplet with a certain weight begins to slide down an inclined surface),[191] and d_w is the wetted diameter (*i.e.* the equivalent diameter of the wetted area at the droplet/GDL interface).

From the above relations, it can be inferred that effective water management can be achieved through an optimum GDL design and a suitable material selection of GDL, because the surface and pore geometry of the GDL will play a critical role in the movement of water droplets throughout its structure. For example, increasing the hydrophobicity of the GDL's surface by coating with materials like PTFE, silica, *etc.* can increase the contact angle (>150°) and decrease the sliding angle (<5°) between the water droplets and GDL surface to facilitate the diffusion of water outside the GDL.[191–193] Furthermore, increasing the pore size of the GDL (*e.g.* > 400 μm radius) can ease the movement of liquid water by decreasing the capillary pressure needed for water removal (eqn (19)).[194,195] In all these, the orientation of fuel cell also plays an important role. In particular, fuel cells arranged in a vertical orientation are found to have better water removal in comparison to the horizontal ones; and this is simply due to gravitational effects.[194] The influence of gravity on water droplet removal is also more prominent on hydrophobic surfaces as compared to hydrophilic surfaces.[192,194]

3.4. Bipolar plates

Bipolar plates are used to provide electrical connection between individual cells in the stack, and these often add a significant weight (~80%) and cost (~45%) to the stack.[196–200] To ensure an adequate connection between individual cells, the bipolar plates should to be strong enough to stand the clamping forces, be thermally stable within the operating range, have a low gas permeability and the ability to uniformly distribute O_2 and H_2 to the GDL, while enabling the removal of the water produced. In addition, the bipolar plates must be resistant to corrosion under the acidic operating conditions of PEMFC.[7,196,200] Other requirements from the manufacturing and commercialization aspects are: low cost, slim and light enough to reduce the stack volume and ensure a low production cycle time.[7,201–204] Technical targets for the bipolar plates as defined by the US DOE for 2020 are summarised in Table 3.[112,205] Various materials such as graphite, aluminium and carbon-polymer composites have been used as bipolar plates.[206–209] In planar fuel cells, owing to the need of reducing weight, the use of a thin flexible Printed Circuit Board (PCB) acting as current collector and bipolar plates is a common practice.[11,13,204] In this case, the PCBs are usually made of fiberglass and to ensure electrical conductivity, these are coated with Cu, Ag or Au.[91,204]

Apart from PCBs, alternatives including gold plated aluminium metallic plates,[9,10] gold-plated 316 stainless steel sheets,[12] copper foils with a conductive layer of gold, and gold-plated stainless-steel nets have also been proposed as bipolar plates for planar fuel cells.[204] The popularity for gold has the electrical conductive layer is due to its higher corrosion resistance to acidic conditions as compared to copper, aluminium and silver.[10] Unlike gold, silver gets tarnished under environmental condition forming compounds such as Ag_2S, AgCl, Ag_2O.[210] Copper sheets along with graphite flow field at both anode and cathode sides have also been used.[204] However, copper is corroded under PEMFC operating condition unless coated with noble metal, *e.g.* gold.[204]

4. Water management and humidification

Water balance in PEMFC is a common issue for the long-term stability and dynamic operation of PEMFC.[211] The most common membrane, Nafion, needs to be hydrated for proton conduction, but excess of water should be avoided because this can affect the capillary breakthrough pressure and lead to a flooding of the cell.[212,213] As previously discussed, to avoid any potential flooding, the cell design as well as the MEA/GDL can be optimised.[214] However, this should be done by taking into account the need for simplicity, minimization of the parasitic power losses, increased reliability, and low costs.[215]

Forner-Cuenca *et. al.* proposed a new approach to making GDL whereby hydrophobic transport pathways are clearly delimited from hydrophilic pathway for water to transport across the fuel cell (Fig. 5).[216] By using such an approach, significant improvement in performance was observed (0.75 V at 0.8 A cm^{-2}) owing to the facilitated mass transport in comparison to commercial GDLs (0.15 V at 0.8 A cm^{-2}).

To facilitate water management, Wang *et. al.* also proposed the use of porous hydrophilic graphite plates treated with titanium dioxide as bipolar plates.[217] The use of a porous carbon flow field structure serving as a wick, *i.e.* a porous material which draws water by capillary action, has also been proposed.[218] In this case, a high air pressure gradient is required to drive water through the wick. Similarly, Pandey *et. al.* proposed the use of hydrophilic materials (carbon cloth, pore size 25–90 μm) as a wick, which covers the entire active layer of the anode or cathode in between MEA and graphite plates.[219] The use of a thin electrically conductive wick (a porous graphite plate 1.5 mm thick, pore diameter 38 mm) placed between the current collector and cathode was also found to facilitate the outflow of water at the cathode without hampering the O_2 supply.[220] In this case, an improved water management was achieved by using a single piece wick, which provided hydraulic paths to the entire cathode area and the oxygen supply was achieved by creating patterns (cut-outs) in the wick.[220] Such a design thus results in two mechanisms: initially when the wick is dry, the capillary forces drive the generated water into the wick and when the collector is saturated with water, it is driven out of the collector by pressure gradient.[220]

5. Planar PEMFC designs

Although the basic requirements and components of all the PEMFC are similar, there are significant variations among the

Table 3 Technical targets for bipolar plates for 2020 set by US Department of Energy (US DOE) for vehicles with the assumption that similar target would apply to portable electronic[112,205]

Characteristics	Units	2020 target
Plate cost	$ per kW	3
Plate weight	kg kW^{-1}	0.4
Plate H_2 permeation coefficient	$cm^3\ cm^{-2}\ s^{-1}$ (@80 °C, 3 atm), 100% RH	1.3×10^{-14}
Corrosion anode	$\mu A\ cm^{-2}$	<1
Corrosion cathode	$\mu A\ cm^{-2}$	<1
Electrical conductivity	$S\ cm^{-1}$	100
Areal specific resistance	$\Omega\ cm^2$	0.01
Flexural strength	MPa	25
Forming elongation	%	40

cells either in the form of the materials used or in the cell design itself. Fuel cells can be designed based on the types of reactants to be supplied and according to the peripheral devices that the system aims to use. In this case, stack arrangement will vary to maximize the current and/or voltage.

5.1 Dead ended anode planar PEMFC

PEMFC with dead end anode provides an opportunity to have maximum (up to 100%) hydrogen utilization because there is no outlet at the anode.[221] In this case, the fuel cell is simpler and less bulky.[222] However, the performance of fuel cells under dead ended mode strongly depends upon the operating conditions, temperature, anode inlet pressure and anode/cathode stoichiometry of reactants, *i.e.* H_2 and O_2. A dead end anode can lead to problems in terms of water management, and thus accelerate carbon corrosion at both the anode and cathode.[223] To avoid this, the hydrogen pressure can be increased to facilitate water transport *via* hydraulic permeation from the anode to cathode side.[224] An alternative option is to install a purge valve at the anode outlet to vent any accumulated water.[225] However, this should be done in ways that help to minimise: (i) hydrogen loss during the purge, (ii) the decrease in voltage output between the purges, (iii) membrane degradation, as a result of the removal of residual water in the MEA due to the gas convection during purging,[226] and (iv) carbon corrosion due to hydrogen starvation over the life cycle of fuel cell operation.[222] Furthermore, during a purge, back diffusion of water from the cathode to anode may affect the recovery time of the maximum cell power output.[226] The exact purge interval and cycle duration highly depend upon the operating conditions.[222] Purging approximately one fourth of the anode gas volume leads to optimal energy efficiency.[227] For a cell operating at 0.6 A cm^{-2}, the purge duration was determined to be of ~0.2 s at the interval of 206.7–238.8 s provided that all the gas can be purged out of anode volume in 0.76 s.[227]

Yang *et. al.* compared the performance of dead-ended anodes with different anode flow field modes, and found that the interdigitated flow field led to the most stable performance due to the better distribution of the reactants (Fig. 6).[228] Anode pressure swing operation has also been reported to be an effective way to minimize water accumulation at the dead ended anode channel as this generates an oscillatory flow of liquid water.[229] Under these conditions with the addition of a water reservoir (Fig. 6), the accumulated water stored can facilitate the hydrogen backflow when the oscillatory flow occurs during pressure swing operation.[223,228] In this case, when the hydrogen supply stops, the drop of local pressure in the anode channels creates a reverse pressure gradient between the anode channels and the outlet reservoir.

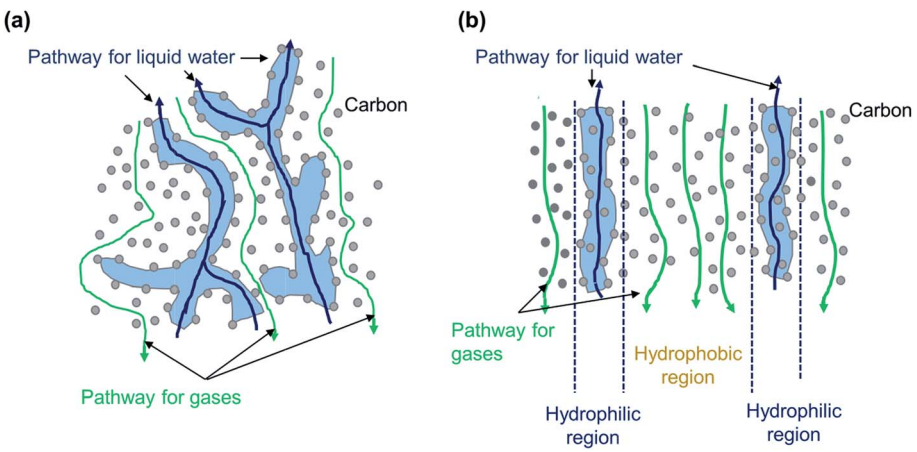

Fig. 5 Illustration of water and gas transport mechanisms through hydrophobic and hydrophilic regions of (a) a conventional GDL, and (b) alternative GDL where both hydrophobic and hydrophilic regions are separated to improve mass transport.[216]

This results in a back flow of hydrogen along with liquid water from the reservoir into the anode channels.

There has not been much work done on planar self-breathing PEMFC operated on dead-ended anode mode. Santarosa *et. al.* reported a performance of 310 mW cm^{-2} at ambient pressure and temperature for an eight cells dead ended-mode stack with air breathing cathodes.[230]

5.2. Conventional planar PEMFC designs

Conventional planar fuel cells have both their anode and cathode end opened to allow the release of unreacted gases and water. Various single cell and stack designs have been proposed with the aim of achieving high durability, high performance, light weight, low stack volume, miniaturisation, flexibility, low fabrication cost and scalability; keeping in mind the need to achieve an optimum power density per weight and volume. An example of conventional planar PEMFC stack is shown in Fig. 7, where the PEMFC stacks (4 to 16 cells put in series) have been fabricated by micro electroforming using copper as bipolar plates with serpentine flow channels.[231] The obtained power density was 100 mW cm^{-2} at 1.7 V for a stack of 2 cells. A volumetric density of 267.8 W L^{-1} and gravimetric density of 53.2 W kg^{-1} was reported for stack of 16 cells.

In conventional planar PEMFC, O_2/air is supplied from a tank or compressor, and this results in an increment in weight and the amount of energy use due to the peripheral devices supplying air/O_2. To address this issue, self-breathing PEMFC designs have been proposed where the cathode is exposed to the environment for a direct supply of O_2. Various innovative arrangements of individual cells and stacks have been proposed for air breathing PEMFC, some of them are summarized in Table 4.

5.3. Air breathing planar PEMFC designs

The designs for air breathing planar PEMFC mainly involve low cost materials such as stainless steel,[12,232] and light PCBs (Fig. 8).[11,13,204,233] Among the current design approaches, durability is addressed by using gold, platinum and niobium plating on stainless steel and copper materials.[12,232,234] The current collectors are graphite, carbons, metal or metal alloys, metal mesh (*e.g.* with an open area of the mesh ranging from 10–80%)[234–240] with a corrosion-resistant surface coating and the sealing gaskets are made from ethylene propylene rubber, silicon, silicon-based rubber, acrylic rubber or thermoplastic elastomers.[237]

In some cases, hydrogen leakage problems were addressed by sealing with silicone the edges of the anode bipolar plate and the MEA interface,[91] and flexibility was achieved by using composite electrodes made of porous carbon nanotubes membranes, carbon paper and polydimethylsiloxane.[48] For example by using these principles, Ning *et. al.* reported a flexible planar PEMFC which retained 89.1% of its performance after bending 600 times.[40,48] A high performing (145.2 mW cm^{-2} in comparison to traditional 90.3 mW cm^{-2}) very thin (0.22 mm) air breathing PEMFC has also been reported, where the anode flow field made of polydimethylsiloxane was attached to the MEA with an adhesive.[48]

In air breathing PEMFC, the design of the stack is critical to ensure sufficient breathing at individual cells. A stack connected in series where the MEA is shared across two cells has been proposed (Fig. 9a).[235] In this configuration, the hydrogen

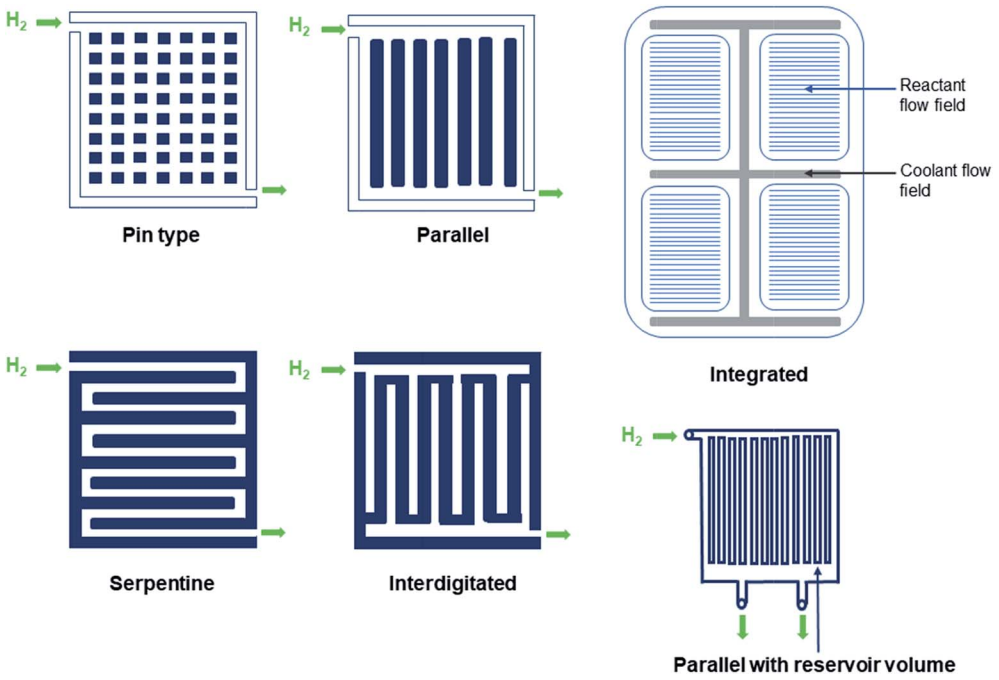

Fig. 6 Different types of flow field designs.[223,230,285,293] The integrated flow field design consists in having both reactant gas flow field and cooling flow field on the same surface.

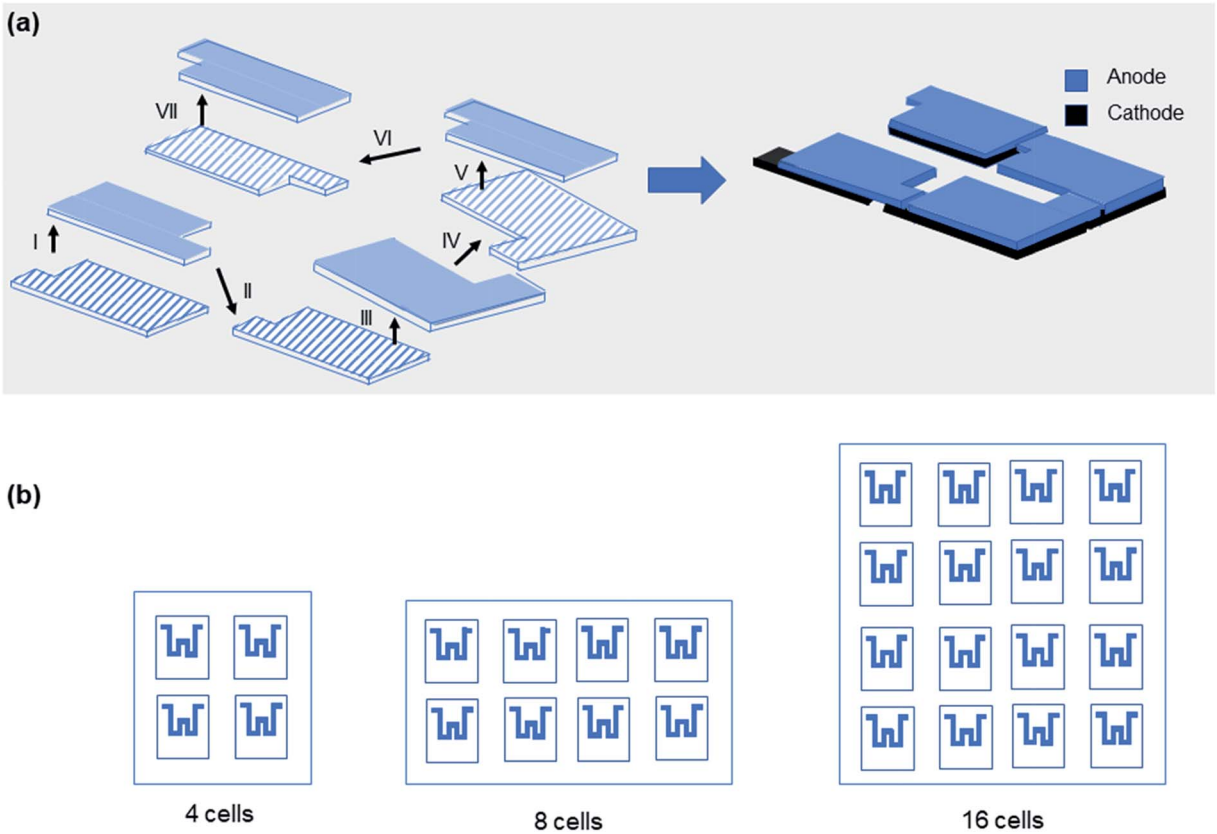

Fig. 7 (a) Proposed assembly of a planar fuel cell stack (4 cell), and (b) resulting array module configuration for 4, 8 and 16 cells.[231]

flow field can also be sandwiched between two open O_2 flow fields (Fig. 9b).[239,240] By using such a configuration, the stack can then be assembled with individual cells in parallel to ensure air/O_2 supply (Fig. 9c).

To maintain reasonable O_2 partial pressure within the stack, it has been proposed to design larger O_2 flow fields in the middle of the stack, because the higher temperature in middle of the stack upon operation leads to a lower partial pressure of O_2.[238] The option of blowing air with a fan attached to the stack is also used as a last resort to improve the amount of supplied O_2 and thus increase the reaction at the cathode.[235,239,240]

6. Manufacturing approaches for making planar PEMFC

A complete planar PEMFC single cell consists of multiple components that need to be manufactured and assembled together. A careful design and manufacturing is important because this will determine the final performance of the fuel cell stack. As previously discussed, three main components must be manufactured to assemble a full PEMFC. These are the MEA, the GDL and the bipolar plates/current collectors.

The assembly of the three components above lead to a single cell, where the MEA is compactly placed between two bipolar plates maintained against each other's by using nuts and bolts. However, in the case of thin planar PEMFC an adhesive made from fluoroelastomers, silicone rubbers, and hydrocarbon-based elastomers is often used.[241]

6.1 Manufacturing of the membrane electrode assembly

As previously discussed, the MEA consists of a catalyst layer, a polymer electrolyte (membrane) and a gas diffusion layer (also called gas diffusion electrode). The catalyst layer is made of a continuous network of ionomer (*e.g.* Nafion) and a catalyst (*e.g.* Pt/C). In this case, the ionomer maintains the transport of protons between the membrane and catalyst. The catalyst layer should also have a porous network for the movement of reactants gases to the catalyst and the removal of water from the catalyst layer.[242]

There are two main methods to fabricate a MEA (Fig. 10).[241] The first one involves the application of the catalyst layer to the GDL followed by the addition of the membrane. The second method relies on the application of the catalyst layer to the membrane followed by GDL addition. The various catalyst deposition methods developed so far are summarised in Table 5, and these include two step methods such as the spraying and the decal transfer method, or a single step deposition method by using sputtering, for example.[243] Due to the lower cost, the two steps method is more common.

Inkjet printing is among the most widely used catalyst deposition techniques. In this case, the catalyst ink is deposited on the substrate of choice by using inkjet printers. High

Table 4 Summary of the various materials used to make air breathing prototype planar PEMFC and their performance

No of cells	Materials for bipolar plates and current collectors	Performances	References
1	Anode: gold plated 316 stainless steel, thickness 10 mm Cathode: gold plated 316 stainless steel, thickness 4 mm	Maximum power density, 124 mW cm^{-2} Stable performance at 200 mA cm^{-2}	12
1	Anode: gold plated stainless steel with gold plated copper current collector Cathode: gold plated Ni mesh	200 mA cm^{-2} (air breathing) 250 mA cm^{-2} (cathodic fan)	232
1	Anode: adhesive copper foil Cathode: three-layer (carbon, a stainless-steel mesh, PCB), with aperture(s) and three different air cathode geometry A: four holes B: single hole C: array of holes)	For A: 305 mW cm^{-2}, obstruction by water droplet For B: 250 mW cm^{-2} For C: 305 mW cm^{-2}	204
6	Anode: dead ended Cathode: slits of opening 10 mm × 1 mm and spacing of 1 mm between the slits Ladder design of stack electrical connection between the cell by Pt wire	10.5 W at 650 mA cm^{-2}	307 and 308
2	Anode and cathode: gold plated Al, thickness of 1.5 mm, cathode opening ratio, 47% Anode placed back to back with insulator in between	With circular opening ~550 mA cm^{-2} Rib distance, 0.87 mm Hydraulic diameter, 4.29 mm	9
2	PCB with copper layer (35 μm) Anode: single channelled serpentine flow field (depth 0.8 mm, ribs width 1 mm) Cathode: parallel, rectangular openings (1.5 mm × 20 mm) at the interval of 1 mm, cathode opening ratio 60%	270 mA cm^{-2}	11, 13 and 309
6	Flexible PCB with Au coated layer Anode: the six single serpentine flow field, 0.5 mm deep, 0.5 mm wide, and separated by 0.5 mm ribs Cathode: various shapes (rectangular, triangular, circular) and opening ratio (22% to 89%)	Best performance, 350 mW cm^{-2} by rectangular shaped (opening ratio 65%)	233
8	Flexible PCB with Au coated layer (thickness 100 μm), stack thickness 3 mm, Anode: flexible PCB current collector Cathode: flexible PCB opening, 65%	Peak power density, 0.2 W cm^{-2} Volumetric power density, 335 W L^{-1}, Gravimetric density, 130 W kg^{-1}	310
1	Anode and cathode bipolar plates: carbon composites with graphite foil (50 μm thick) Current collectors: cupper plates Sealing material: silicone adhesive applied between the anode bipolar plate and the membrane	Power density: 0.41 W cm^{-2} Gravimetric density: 590 W kg^{-1}	91
10	Anode and cathode: monopolar design Flow field plates: acrylonitrile–butadiene–styrene	Power density, 99 mW cm^{-2} Corrosion resistance	10

Table 4 (*Contd.*)

No of cells	Materials for bipolar plates and current collectors	Performances	References
	Fabrication by additive manufacturing Ribs (current collectors): copper coated with gold	Faster and cheaper manufacturing technology	

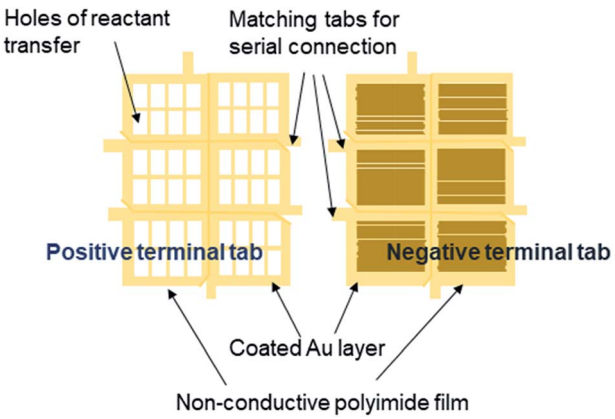

Fig. 8 Example of an Au coated flexible printed circuit board current collector.[233]

utilization of precious catalyst (Pt) can be achieved with this method. Other advantages include a short production time, low production cost and good reproducibility.[244] However, the initial capital cost of a printing system can be high. Some of the examples reported in the literature include rapid ink jet printing to deposit a Co_3O_4/N-rGO-based catalyst layer on carbon substrates.[245] In this case, a thin catalyst film (1.5–2 μm) with a loading of 0.026 mg(Pt) cm^{-2} was achieved for both the anode and cathode electrodes.[246]

By spraying technique, the catalyst slurry is sprayed on the substrate. The advantages of spraying include scalability and the possibility to quickly cover large areas. In addition, the initial capital cost is low. The spraying systems can be based on air assisted cylindrical liquid jet spraying methods, where the catalyst ink is atomized by an air stream before spraying.[199] Electro-spraying is also a popular approach,[247–249] whereby the catalyst ink deposition is done under the influence of a strong electric field.[248] In this case, upon an electrical potential difference between the substrate (electrode) and the discharge needle, the catalyst ink breaks through the needle in the form of a spray of charged particles (droplets).[248,250,251] The applied electric field then drives the charged droplets towards the substrate to be coated at a flow rate determined by the intensity of the electrical field (*e.g.* 0.4–0.6 mL h^{-1}).[248] It should be noted that by electro-spraying, the deposited catalysts often display better performances (power output of 441 mW cm^{-2}) compared to air sprayed catalysts (327 mW cm^{-2}).[249] A possible reason for such a better performance is the efficient distribution of ionomer within the mesoporous structure of the catalyst layer.[249]

Methods based on both ink jet printing or spraying rely on the preparation of an appropriate catalyst ink. A typical ink composition is Pt/C (20 wt%, 0.4 mg cm^{-2}), PTFE (30% of the mixture) and a solution of Nafion (5 wt%, 2 mg cm^{-2}).[252] In this case, Nafion provides proton conduction within the catalyst layer. Hence, low Nafion content result in poor H^+ conductivity and in contrast high Nafion content creates barriers for O_2 and H_2 diffusion within the MEA.[253] An appropriate amount of ionomer is thus crucial for the optimum cell operation, and by electrospray deposition a 15% Nafion content was found to be ideal.[254]

Physical methods such as sputtering, pulse laser deposition have also been investigated to achieve low and uniform Pt deposition. For example, radio frequency sputtering has been used to deposit ultra-low amounts of Pt ~0.0011 to 0.06 mg cm^{-2} and under these conditions the fuel cell achieved 297 mW cm^{-2} under a H_2/O_2 feed.[255] A lower power of 124 mW cm^{-2} with a Pt loading of 0.005 mg cm^{-2} have also been reported by other groups.[256] Fuel cells of such a low power output could be relevant to low-cost applications involving micro-electronic systems and sensors. The ideal amount of ionomer loading on the substrate by the sputtering approach was found to be ≤1.5 mg cm^{-2}.[256] Higher amounts of ionomer is not desirable as it can cover the catalyst particles.[257]

The use of atomic layer deposition has also been reported. For example, Pt thin film electrodes have been deposited at the surface of SiO_2 nanofibers by using methylcyclopentadienyl trimethyl platinum ($MeCpPtMe_3$) as the Pt precursor in an argon/hydrogen mixture. By this deposition method, a Pt loading of 0.1 mg cm^{-2} was achieved and the fuel cell reached ~1 A cm^{-2} at 0.4 V.[258] Similarly, deposition of Pt nanocrystals at a carbon nanotube/graphene hybrid structure led to a current density of ~800 mA cm^{-2} at 0.45 V and 75 °C for a Pt loading of 81 μg cm^{-2}. In this particular case, Pt was deposited by atomic layer deposition at 0.81 μg cm^{-2}, and this was repeated 100 times to achieve the required thickness.[259]

By pulsed laser deposition technique, a Pt loading of 17 μg cm^{-2} at the anode and 100 μg cm^{-2} at the cathode was reported. The resulting fuel cell delivered 674 mW cm^{-2} at 0.6 V.[260] In this case, it was found that the thin catalyst layer obtained by pulsed laser deposition did not require any ionomer for improving the proton conductivity. This is because the Pt particles deposited by this method are located on the surface of the support and thus very close to the Nafion membrane when assembled into a MEA.[260]

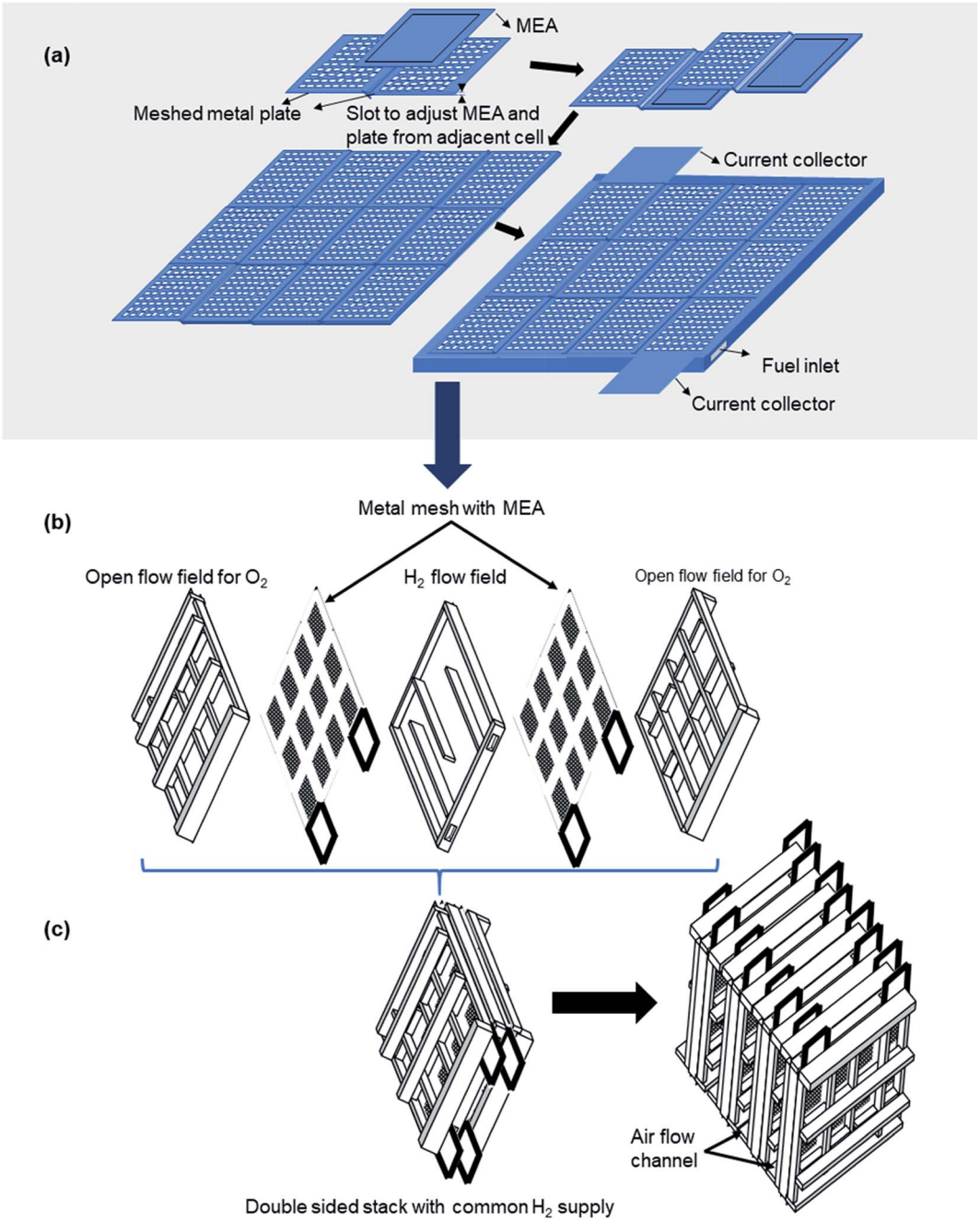

Fig. 9 (a) Example of assembly of planar fuel cell in series with the MEA shared across two cells,[235] (b) exploded view of a two planar cells sharing the same hydrogen flow field, and (c) example of stack assembly of (b) in parallel to allow for air flow from the side of the stack.[239,240]

6.2. Manufacturing of the gas diffusion layer

Effective preparation of the GDL is important as this directly affects the performance of the fuel cell.[261] The ideal method for manufacturing a GDL should lead to a high Gurley number (corresponding to the flow resistance), a large number of micropores for water management, uniform thickness and ease in scaling up.[262–264] As discussed above, the GDL should consist of a microporous layer developed on the surface of a macroporous substrate.[254] A general GDL manufacturing process is as follows:[265] A solvent (alcohol or isopropanol), a dispersant (anionic surfactant or a cationic surfactant), and an aqueous polymer resin are added to a carbon powder (particle size 20–2000 nm) and mixed to prepare a dispersed solution. Further fluorinated resin (PTFE, ~5% per wt of carbon powder) suspension is added to the above mixture and coated on a macroporous carbon substrate (usually pre-treated with a PTFE solution) to form a primer layer. The microporosity is then further developed by additional coating with the above slurry until the desired thickness is obtained (generally 20 to 200 μm).[265] The resulting product is thermally treated at 350 °C to

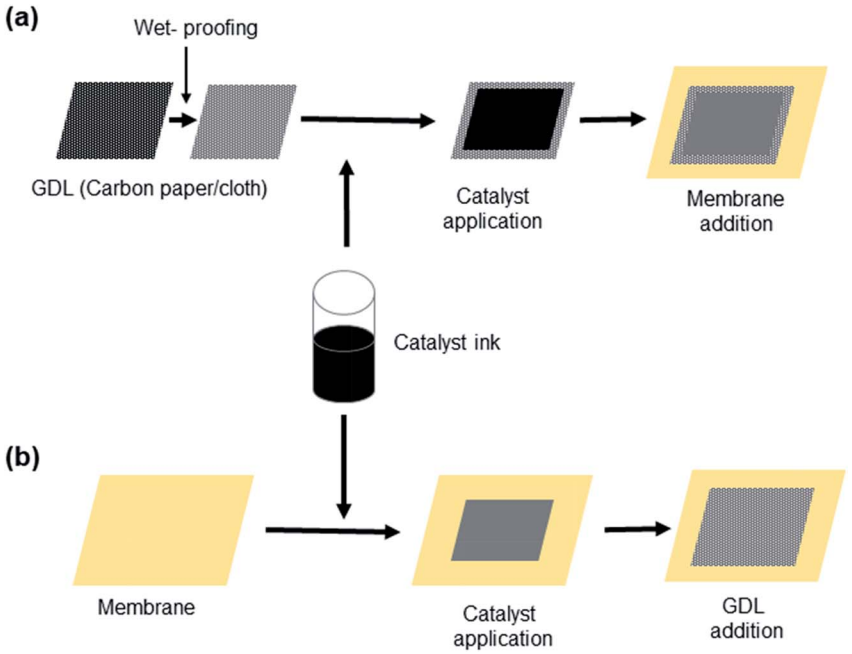

Fig. 10 Common approaches for fabricating MEA with the catalyst deposited first on (a) the GDL, and (b) the membrane.

Table 5 Summary of current methods for catalyst loading during MEA manufacturing[245,250,311–315]

Deposition	Technique of deposition	Amount of catalyst loaded (μg cm^{-2})
Coating method	Brush coating on proton conducting membrane	70–170
	Screen printing of catalyst slurry	300 ± 10
	Doctor blade	400
	Slot die coating	310 ± 63
	Decal transfer	4000
	Inkjet printing	21–500
Vapour deposition method	Sputtering techniques	1–700
	Ion beam	17
	Pulsed electrodeposition	25
	Electrospray	10–300
	Electrospinning	0.877
Ultrasonic spray		50

give the final GDL. Mixture of two types of carbons has also been used to prepare a GDL. For example, a bi-functional pore structure (made with 20 wt% black pearls 2000 and 80 wt% acetylene black carbon) was reported to led to some improvement in water transport because of the varied porosity in the resulting GDL.[266]

The microporous layer plays an important role in improving the PEMFC performance and water management as the micropores can act as a buffer to prevent both drying and flooding.[267,268] Another factor that plays an important role in the performance of fuel cell is the thickness of the GDL.[269] A thinner GDL is preferable as this can provide shorter distances for the diffusion of reactants.

The most common methods for the preparation of GDLs are those based on wet techniques like spraying and screen printing (Fig. 11).[270–272] In both techniques, the ink composition is same with the only difference coming from higher amounts of suspension agents (polyethylene oxide, PTFE, *etc.*) in case of screen printing and the addition of a few drops of polyethylene glycerol *p*-iso-octylphenyl ether (Triton X-100) as surfactant to increase the viscosity of the ink.[273] Currently, a hybrid fabrication method is used. The diffusion layer is prepared by spraying technique and the catalyst layer by screen printing technique (Fig. 11).[261,273]

Comparison of the three basic preparation methods of spraying, vacuum-filtration and screen printing on the final properties of GDLs are summarised in Table 6. Commercial GDLs have marginal values of Gurley number indicating low gas permeability.[263,264] Although spraying and vacuum filtration methods lead to higher Gurley numbers, these methods have other issues such as low reproducibility and result in a lack of

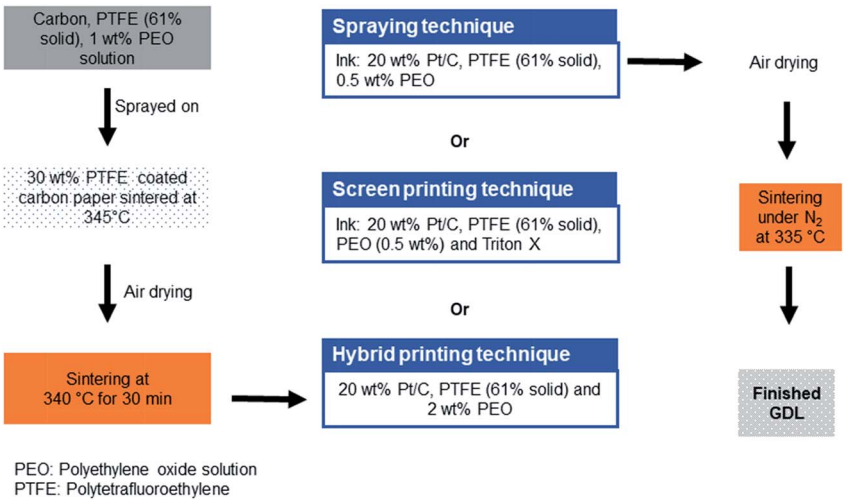

Fig. 11 Flow chart of fabrication of GDL by spraying technique, screen printing technique and hybrid spraying/screen printing technique.[261,273]

Table 6 Comparison of the Gurley number obtained for GDL prepared by depositing a carbon/PTFE ink on carbon substrates (carbon paper or carbon cloths with a porosity of 69.9–74.4%).[262–264] Carbon and PTFE loading in all the three methods are 1.5 mg cm^{-2}

Gas diffusion layers	Gurley number (L min^{-1}) (cm water × cm^2)$^{-1}$	Resistivity (mΩ cm)
Spraying	0.50	—
Vacuum-filtration	0.25	—
Silk-screening	0.16	4
Commercial (E-TEK)	0.02–0.04	5–20

micropores. Spraying leads to excessive roughness, large cracks. Vacuum filtration is difficult to scale up. To date, screen printing is the best method for carbon loading because it leads to at least four times more gas permeability than the commercial GDL (ETEK cloth, V.2.20).[263]

Apart from the above methods, GDL's preparation has also been done by coating process, *e.g.* blade and wire coating.[274,275] For example, wire wound rod can be used to fabricate a microporous layer on a non-woven macroporous carbon paper. The process is semi-automated with a single pass and the carbon loading within the microporous layer can be varied between 2.5 and 3.0 mg cm^{-2}.[274]

The present need is in the development of GDLs with self-adjusting functionalities of water retention and water draining along with a steady supply for reactant gases to the catalyst layer. These improvements should occur while ensuring good electrical conductivity, low cost, as the cost of GDLs is about 20% that of the MEA and about 5% that of the overall fuel cell stack.[276]

The use of superhydrophobic materials (with contact angles > 150)[277] in GDLs has been reported to assist with water removal. However, excessive and quick removal of water from the cell can impact the water retention of the membrane and the overall performance of the fuel cell. It is important that both hydrophilicity and hydrophobicity are balanced to ensure an optimum fuel cell performance.[278]

One of the approaches to address the problem of electrical conductivity and reduce manufacturing time is in the development of a GDL where the carbon ink to create the microporosity is only applied once.[279] In this case, carbon black, vapour grown carbon fibres and graphene are mixed in ethanol followed by addition of a PTFE dispersion. After removal of the ethanol, the mixture is pressed and sintered at 130 °C to obtain the GDL. The presence of graphene improves the electrical conductivity (resistivity, 3.71×10^{-3} Ω cm) in comparison to commercial SGL 35BC (1.06×10^{-3} Ω cm).[279] In addition, developing patterns on commercial GDLs using a laser beam or chemical treatment with H_2O_2/H_2SO_4 has also been reported to improve the electrical conductivity of GDLs.[280]

6.3. Manufacturing of bipolar plates

Bipolar plates can be made of metals, non-metals and composites. In the case of polymeric based bipolar plates (where conductivity can be achieved by adding conductive additives such as graphite and graphene), several fabrication methods have been proposed. This includes the fabrication of composite bipolar plates by compression, injection, injection–compression moulding, two components injection and perform moulding.[281,282] For example, mixtures of vinyl ester resin, fluorochemical intermediates (*e.g.* fluoroalkylacrylates and fluoroalkylolefins) for surface hydrophobicity, graphite powder (20 to 95% wt and 80 to 325 mesh), carbon black (0 to 5% wt), and carbon fibres (<1 mm in length) have been used to fabricate bipolar plates.[282]

In compression moulding, the desired materials (*e.g.* graphite and polymers) are mixed together and dried at ~70 °C. The dried mixture is milled to form a powder which is then injected into the heated mould.[281,283] During this process, the use of a low mould pressure (1.5 MPa) was found to be better to enhance the porosity of the bipolar plate surface and facilitate water absorption.[284] However, the moulding pressure should not be too low as to ensure good electrical conductivity across the bipolar plate.[284]

Injection moulding is a common method suited for mass production where the polymer in the form of granules/pellets is

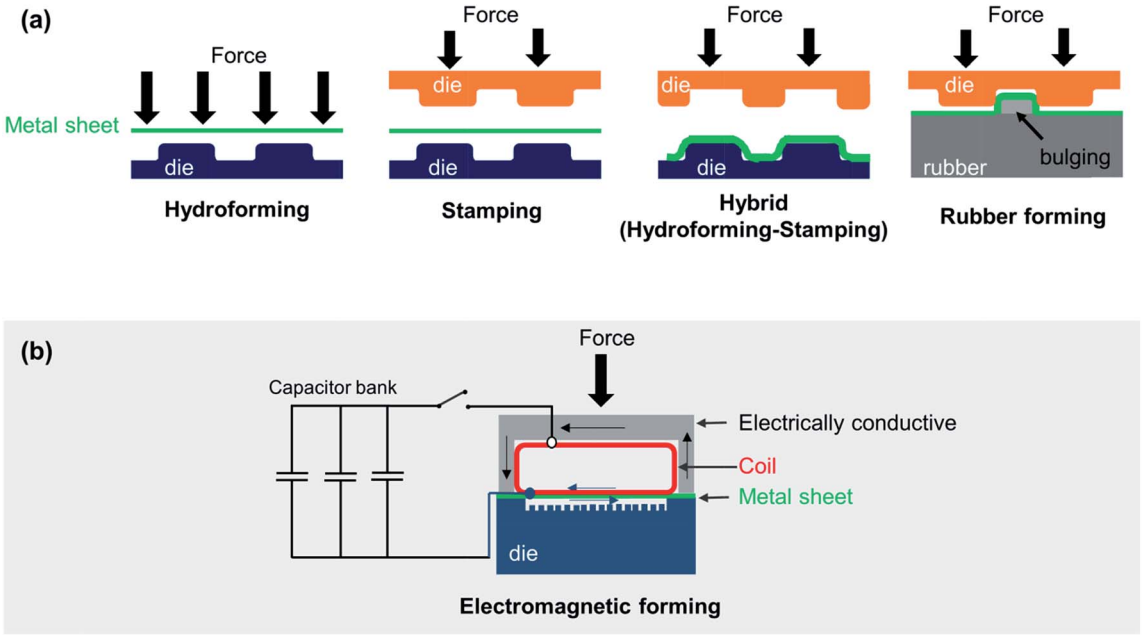

Fig. 12 Methods of developing micro-channels by (a) hydroforming, stamping, hydroforming-stamping and rubber forming, and (b) electromagnetic forming.[208,274–276]

melted before injection into a chamber formed by a split-die mould.[208,281] In case of preform moulding, a conductive composite material is heated outside the mould to a temperature above the melting point and inserted to the cold mould for shaping.[281]

Often metallic bipolar plates are preferred over plastic based bipolar plates, because of advantages including high conductivity, formability, low gas permeability and excellent mechanical properties.[208] But metallic bipolar plates can undergo corrosion.[285] Iron based stainless steel and titanium are often

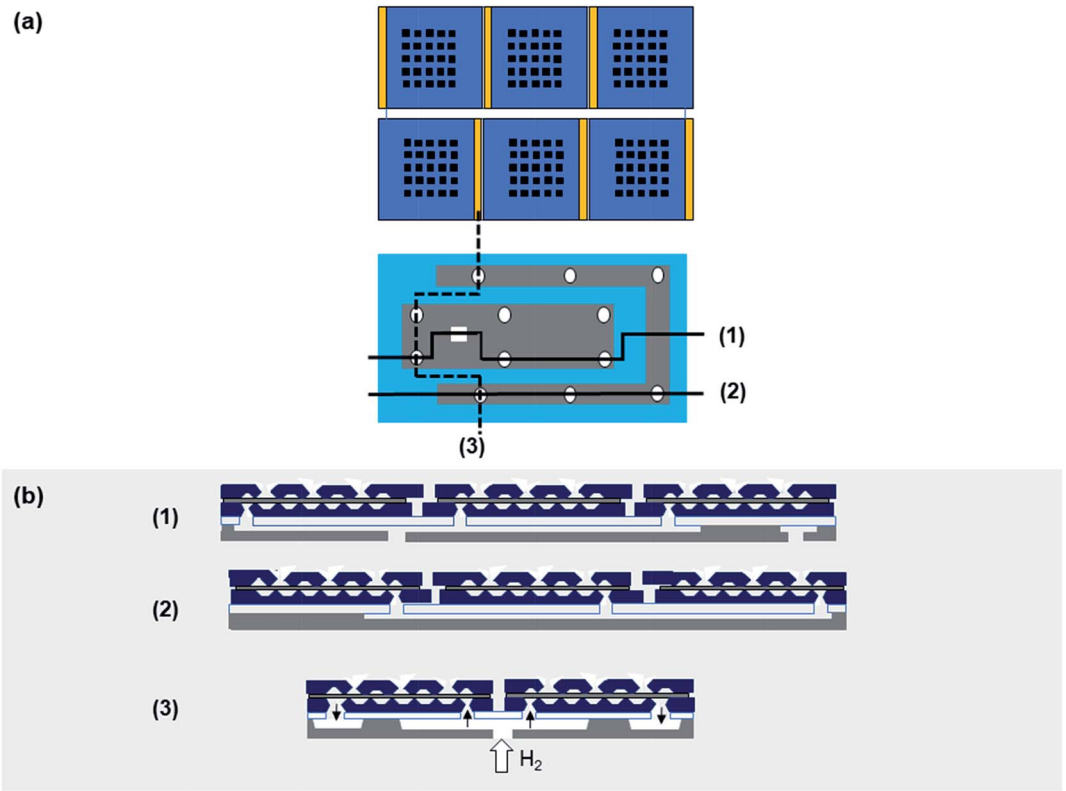

Fig. 13 Six celled stack of PEMFC based on MEMS manufacturing (a) top view, and (b) cross section along (1), (2) and (3).[297]

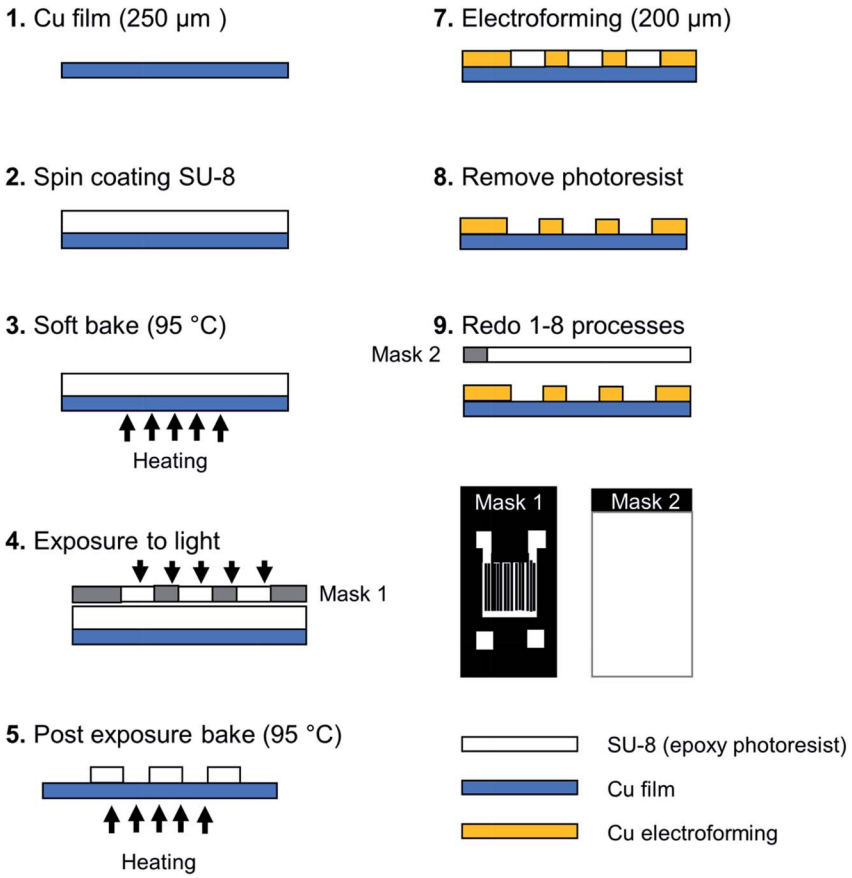

Fig. 14 Steps for the micro-fabrication of flow field by ultraviolet lithography.[294]

the preferred solution due to their low cost and relative good corrosion resistance.[285] However, the corrosion resistance of stainless steel in acidic condition is lower (corrosion current density of 8.9 μA cm^{-2})[286] to that of titanium (corrosion current density of 0.042 μA cm^{-2}).[287] Coating stainless steel with metal nitrides, *e.g.* TiN, CrN *etc.*,[288,289] has been shown to improve resistance to corrosion (*e.g.* to ~0.2 μA cm^{-2})[286] due to high stability of nitrides under acidic conditions and the formation of protective and stable oxide layers, *e.g.* TiO_2, Cr_2O_3.[290] Methods including stamping, hydroforming, hybrid (hydroforming–stamping), electromagnetic forming and rubber forming can then be used to develop micro-channels within these thin metal sheets to support gas and water flow (Fig. 12).[208,285,291,292] The micro channels can take various forms including pin-type flow field, series–parallel flow field, serpentine flow field, interdigitated flow field and integrated flow field (Fig. 6).[285,293]

Recently, few machine-based manufacturing technologies have been developed to fabricate bipolar plates for miniature planar PEMFC. These include Micro-Electro-Mechanical Systems (MEMS) and additive manufacturing also known as 3D printing.[10,294–305] In MEMS, the bipolar plates can be fabricated by micromachining various materials such as silicon, metals, and polymers. An example of six celled stack PEMFC based on MEMS manufacturing is shown in Fig. 13.[297]

Additive manufacturing can be used to directly produce three dimensional parts with a complete freedom of design. Some of the advantages of this method are a reduced manufacturing time and a reduction in waste. Additive manufacturing can be used to make bipolar plates from various materials such as ceramics, glass, metals, polymers, graphene and composite materials (*e.g.* acrylonitrile butadiene styrene and carbon nanotubes).[300] Other fabrication methods for making bipolar plates include the use of micro-fabrication processes employing deep ultraviolet lithography to develop the flow field(Fig. 14).[294]

7. Conclusions and perspectives

With the drastic reduction in the cost of photovoltaic, the possibility of realising economies based on 100% renewables seems less distant. In this context, hydrogen technologies are key enablers. In particular, fuel cells have been identified as one of the most promising technology for the conversion of hydrogen into electricity because of their ability to operate continuously as long as hydrogen is supplied. Additional advantages of fuel cells include silent operation, little moving parts and relativity fast-starting time.

Among the various fuel cells, PEMFC are already commercialized products with application ranging from stationary

electricity generation, to portable and vehicle applications. However, mass scale manufacturing of PEMFC is still challenging because of the lack of a global market and the level of investment required to reach full automation. The relative high cost of various components of PEMFC and long-term durability are also limiting factors for the mass market penetration of the technology.

Beyond the large market of fuel cell vehicles, fuel cells could also find application in many of the portable electronics at the basis of the digitalisation of our economies. Recent progress on planar PEMFC in air breathing mode provide paths for light, low cost small fuel cells stack of high volumetric power density. However, several challenges remain to bring cost down, engineer and design better stack assemblies and develop effective manufacturing processes to produce planar PEMFC at scale.

Although, there has been some achievements in cost reduction along bipolar plates and current collectors, the major source of cost still remains that of the Pt catalyst and the Nafion membrane. Significant efforts have been made to increase the catalytic activity and reduce Pt loading by alloying Pt with other metals and controlling atomic arrangement in the nanocatalyst but for the broad utilisation of planar PEMFC, Pt should be fully replaced by cheaper and more abundant alternatives. Transition metal–nitrogen–carbon catalysts have shown good performance for ORR and could be one of the potential candidates to replace Pt. However, the performance of such catalyst at commercial scale still remains an open question.

The replacement of perfluorinated type membranes (Nafion) is the other challenge. These membranes remain expensive and suffer issues including long-term durability, low operating temperature, and poor performance at low humidity levels. Recent development of membranes from aromatic polymers, polyphenylene and composite materials (*e.g.* arylene ether sulfone and perfluorosulfonic acid) have given some optimism regarding cost reduction, high temperature operation and higher water uptake capacity. However, the combination of all these features in a single membrane has not been achieved yet. Also, the performance of these membranes in operating fuel cells and long-term durability is still to be observed. Although the membrane requirement for all types of PEMFC is the same, the ideal membrane for air breathing planar PEMFC should provide high proton conductivity even at reduced hydration levels since membrane dehydration will occur due to open air cathode configuration. In addition, for the large-scale deployment of PEMFC, alternative membranes of superior performance as compared to Nafion and lower cost of manufacturing are desirable.

In terms of stack design and engineering, mass flow management of gases and water is an important issue as this dictates the overall performances of the final fuel cell assembly. With current know-how, the polymer electrolyte membrane needs hydration to conduct protons but an excess of water will block the path for the reactants resulting in performance degradation and flooding of the catalyst layer. Membranes requiring low hydration and able to operate at higher temperature can address this issue as at elevated temperatures, removal of water vapour is easier as compared to liquid water. However, in a planar fuel cell configuration for portable electronic, elevated temperatures should be avoided to preserve the electronic and optimise energy use, and thus proton conductors that can operate across a wide temperature window (−10 to 50 °C), while ensuring appropriate removal of the water still remain to be developed. In this respect, the development of better multifunctional materials and GDL concepts are required both in terms of management of reactants and by-products of the fuel cell reaction but also in terms of electronic conduction. This is particularly important for developing better planar fuel cells owing to the requirement of optimising the power output per stack volume and weight.

Manufacturing methods should also be progressed to enable the reliable and accurate production of fuel cell systems at scale with efficiencies approaching that recorded at the laboratory scale. For example, there have been some important achievements in identifying methods to develop catalytic layers both on membranes and GDLs with good performances even at low catalyst loading. Assuming that these fuel cells based on low catalyst loading can be further improved to minimise side reactions including that of catalyst leaching, such findings should be more rapidly translated towards large scale manufacturing. With the emergence of additive manufacturing methods there has been some progress made in the fabrication of various fuel cell components, but the bottleneck remains in the assembly of individual components into a fuel stack. Automation can help to some extent, but robotic arms assembling the bipolar plates, GDL and MEA have a limited output in comparisons to roll to roll processes. Improved fabrication methods remain critical for the mass production, penetration and widespread use of planar fuel cells across electronic goods. If these can be resolved along the development of better materials, it can be anticipated that planar PEMFC in conjunction with advanced hydrogen storage technologies may become the norm to power a digital society.

Conflicts of interest

No conflict of interest.

References

1 I. Dincer and C. Acar, *Int. J. Hydrogen Energy*, 2015, **40**, 11094–11111.
2 J. Andersson and S. Grönkvist, *Int. J. Hydrogen Energy*, 2019, **44**, 11901–11919.
3 Y. H. Sun, C. Q. Shen, Q. W. Lai, W. Liu, D. W. Wang and K. F. Aguey-Zinsou, *Energy Storage Materials*, 2018, **10**, 168–198.
4 J.-H. Wee, *Renewable Sustainable Energy Rev.*, 2007, **11**, 1720–1738.
5 Á. Varga, in *Introduction to Fuel Cell Technology, Fuel Cell Electronics Packaging*, ed. K. Kuang, and K. Easler, Springer Science & Business Media, Boston, M.A., 2007, ch. 1, pp. 1–32.
6 P. Sapkota and H. Kim, *J. Ind. Eng. Chem.*, 2009, **15**, 445–450.

7 J. Larminie and A. Dicks, *Fuel Cell Systems Explained*, Wiley, England, 2005.
8 J. M. Nail, G. Anderson, G. Ceasar and C. J. Hansen, *The Evolution of the PEM Stationary Fuel Cell in the U.S. Innovation System*, U.S. Patents and Trademark Office (U.S. PTO), Washington, DC, 2003.
9 N. Bussayajarn, H. Ming, K. K. Hoong, W. Y. Ming Stephen and C. S. Hwa, *Int. J. Hydrogen Energy*, 2009, **34**, 7761–7767.
10 C. Y. Chen, W. H. Lai, B. J. Weng, H. J. Chuang, C. Y. Hsieh and C. C. Kung, *J. Power Sources*, 2008, **179**, 147–154.
11 A. Schmitz, M. Tranitz, S. Wagner, R. Hahn and C. Hebling, *J. Power Sources*, 2003, **118**, 162–171.
12 T. Hottinen, M. Mikkola and P. Lund, *J. Power Sources*, 2004, **129**, 68–72.
13 A. Schmitz, S. Wagner, R. Hahn, H. Uzun and C. Hebling, *J. Power Sources*, 2004, **127**, 197–205.
14 H. S. Johnston and C. Parr, *J. Am. Chem. Soc.*, 1963, **85**, 2544–2551.
15 J. Zhang, *PEM Fuel Cell Electrocatalysts and Catalyst Layers, Fundamentals and Applications*, Springer-Verlag London, London, 2008.
16 J. Erlebacher, *Solid State Phys.*, 2009, **61**, 77–141.
17 A. Appleby, in *Encyclopedia of Electrochemical Power Sources*, Elsevier, Amsterdam, 2009, vol. 2, pp. 810–852.
18 K. Li, Y. Li, Y. Wang, F. He, M. Jiao, H. Tang and Z. Wu, *J. Mater. Chem. A*, 2015, **3**, 11444–11452.
19 M. L'Her, in *Encycl. Electrochem.*, Wiley-VCH Verlag GmbH & Co. KGaA, Weinheim, 2007.
20 E. S. Davydova, S. Mukerjee, F. Jaouen and D. R. Dekel, *ACS Catal.*, 2018, **8**, 6665–6690.
21 W. C. Sheng, H. A. Gasteiger and Y. Shao-Horn, *J. Electrochem. Soc.*, 2010, **157**, B1529–B1536.
22 S. Alayoglu, A. U. Nilekar, M. Mavrikakis and B. Eichhorn, *Nat. Mater.*, 2008, **7**, 333–338.
23 T. Tsuneda, R. K. Singh, A. Iiyama and K. Miyatake, *ACS Omega*, 2017, **2**, 4053–4064.
24 Z. Lu, G. Chen, S. Siahrostami, Z. Chen, K. Liu, J. Xie, L. Liao, T. Wu, D. Lin, Y. Liu, T. F. Jaramillo, J. K. Nørskov and Y. Cui, *Nat. Catal.*, 2018, **1**, 156–162.
25 S. Siahrostami, A. Verdaguer-Casadevall, M. Karamad, D. Deiana, P. Malacrida, B. Wickman, M. Escudero-Escribano, E. A. Paoli, R. Frydendal, T. W. Hansen, I. Chorkendorff, I. E. Stephens and J. Rossmeisl, *Nat. Mater.*, 2013, **12**, 1137–1143.
26 I. Katsounaros, W. B. Schneider, J. C. Meier, U. Benedikt, P. U. Biedermann, A. A. Auer and K. J. Mayrhofer, *Phys. Chem. Chem. Phys.*, 2012, **14**, 7384–7391.
27 V. A. Sethuraman, J. W. Weidner, A. T. Haug, S. Motupally and L. V. Protsailo, *J. Electrochem. Soc.*, 2008, **155**, B50–B57.
28 J. Divisek, H. Schmitz and B. Steffen, *Elecmchimica Acta*, 1994, **39**, 1723–1731.
29 S. Taylor, E. Fabbri, P. Levecque, T. J. Schmidt and O. Conrad, *Electrocatalysis*, 2016, **7**, 287–296.
30 C. H. Choi, H. C. Kwon, S. Yook, H. Shin, H. Kim and M. Choi, *J. Phys. Chem. C*, 2014, **118**, 30063–30070.
31 E. M. Karp, C. T. Campbell, F. Studt, F. Abild-Pedersen and J. K. Nørskov, *J. Phys. Chem. C*, 2012, **116**, 25772–25776.
32 J. K. Norskov, J. Rossmeisl, A. Logadottir, L. Lindqvist, J. R. Kitchin, T. Bligaard and H. Jonsson, *J. Phys. Chem. B*, 2004, **108**, 17886–17892.
33 N. Wagner, W. Schnurnberger, B. Muller and M. Lang, *Electrochim. Acta*, 1998, **43**, 3785–3793.
34 M. Schalenbach, M. Zillgitt, W. Maier and D. Stolten, *ACS Appl. Mater. Interfaces*, 2015, **7**, 15746–15751.
35 L. M. Roen, C. H. Paik and T. D. Jarvic, *Electrochem. Solid-State Lett.*, 2004, **7**, A19–A22.
36 N. Macauley, D. D. Papadias, J. Fairweather, D. Spernjak, D. Langlois, R. Ahluwalia, K. L. More, R. Mukundan and R. L. Borup, *J. Electrochem. Soc.*, 2018, **165**, F3148–F3160.
37 J. Chen, J. B. Siegel, T. Matsuura and A. G. Stefanopoulou, *J. Electrochem. Soc.*, 2011, **158**, B1164–B1174.
38 A. Husar, S. Strahl and J. Riera, *Int. J. Hydrogen Energy*, 2012, **37**, 7309–7315.
39 H. A. Gasteiger and N. M. Markovic, *Science*, 2009, **324**, 48–49.
40 Y. Wang, K. S. Chen, J. Mishler, S. C. Cho and X. C. Adroher, *Appl. Energy*, 2011, **88**, 981–1007.
41 G. S. Harzer, A. Orfanidi, H. El-Sayed, P. Madkikar and H. A. Gasteiger, *J. Electrochem. Soc.*, 2018, **165**, F770–F779.
42 K. Jiang, D. Zhao, S. Guo, X. Zhang, X. Zhu, J. Guo, G. Lu and X. Huang, *Sci. Adv.*, 2017, **3**, e1601705.
43 A. Kraytsberg and Y. Ein-Eli, *Energy Fuels*, 2014, **28**, 7303–7330.
44 B. E. Logan, B. Hamelers, R. Rozendal, U. Schroder, J. Keller, S. Freguia, P. Aelterman, W. Verstraete and K. Rabaey, *Environ. Sci. Technol.*, 2006, **40**, 5181–5192.
45 A. B. Stambouli and E. Traversa, *Renewable Sustainable Energy Rev.*, 2002, **6**, 433–455.
46 Z. Shao and M. O. Tade, *Intermediate-Temperature Solid Oxide Fuel Cells: Materials and Applications*, Springer-Verlag Berlin Heidelberg, Berlin, 2016.
47 O. A. Obeisun, Q. Meyer, J. Robinson, C. W. Gibbs, A. R. Kucernak, P. R. Shearing and D. J. L. Brett, *Int. J. Hydrogen Energy*, 2014, **39**, 18326–18336.
48 F. Ning, X. He, Y. Shen, H. Jin, Q. Li, D. Li, S. Li, Y. Zhan, Y. Du, J. Jiang, H. Yang and X. Zhou, *ACS Nano*, 2017, **11**, 5982–5991.
49 T. Park, Y. S. Kang, S. Jang, S. W. Cha, M. Choi and S. J. Yoo, *NPG Asia Mater.*, 2017, **9**, e384.
50 M. Y. Karidurаganavar, R. K. Nagarale, A. A. Kittur and S. S. Kulkarni, *Desalination*, 2006, **197**, 225–246.
51 R. K. Nagarale, G. S. Gohil and V. K. Shahi, *Adv. Colloid Interface Sci.*, 2006, **119**, 97–130.
52 V. Rao, N. Kluy, W. Ju and U. Stimming, in *Handbook of Membrane Separations: Chemical, Pharmaceutical, Food and Biotechnological Applications*, eds. A. K. Pabby, S. S. H. Rizvi and A. M. S. Requena, Taylor and Francis group, UK, 2015, ch. 21, pp. 567–614.
53 P. Choi, N. H. Jalani and R. Datta, *J. Electrochem. Soc.*, 2005, **152**, E123–E130.
54 D. K. Paul, R. McCreery and K. Karan, *J. Electrochem. Soc.*, 2014, **161**, F1395–F1402.
55 S. J. Peighambardoust, S. Rowshanzamir and M. Amjadi, *Int. J. Hydrogen Energy*, 2010, **35**, 9349–9384.

56 A. Z. Weber and J. Newman, *J. Electrochem. Soc.*, 2003, **150**, A1008–A1015.
57 N. C. Osti, T. N. Etampawala, U. M. Shrestha, D. Aryal, M. Tyagi, S. O. Diallo, E. Mamontov, C. J. Cornelius and D. Perahia, *J. Chem. Phys.*, 2016, **145**, 224901.
58 A. V. Anantaraman and C. L. Gardner, *J. Electroanal. Chem.*, 1996, **414**, 115–120.
59 S. Feng and G. A. Voth, *J. Phys. Chem. B*, 2011, **115**, 5903–5912.
60 K. Jiao and X. Li, *Prog. Energy Combust. Sci.*, 2011, **37**, 221–291.
61 H. Gao and K. Lian, *RSC Adv.*, 2014, **4**, 33091–33113.
62 X. Ling, M. Bonn, S. H. Parekh and K. F. Domke, *Angew. Chem., Int. Ed. Engl.*, 2016, **55**, 4011–4015.
63 T. Ishimoto and M. Koyama, *Membranes*, 2012, **2**, 395–414.
64 C. Francia, V. S. Ijeri, S. Specchia and P. Spinelli, *J. Power Sources*, 2011, **196**, 1833–1839.
65 K. D. Kreuer, *J. Membr. Sci.*, 2001, **185**, 29–39.
66 V. Mehta and J. S. Cooper, *J. Power Sources*, 2003, **114**, 32–53.
67 A. S. Arico, D. Sebastian, M. Schuster, B. Bauer, C. D'Urso, F. Lufrano and V. Baglio, *Membranes*, 2015, **5**, 793–809.
68 C. Fiori, A. Dell'Era, F. Zuccari, A. Santiangeli, A. D'Orazio and F. Orecchini, *Int. J. Hydrogen Energy*, 2015, **40**, 11949–11959.
69 K. M. Nouel and P. S. Fedkiw, *Electrochim. Acta*, 1998, **43**, 2381–2387.
70 M. A. Haque, A. B. Sulong, R. E. Rosli, E. H. Majlan, L. K. Shyuan and M. A. A. Mashud, *2015 Ieee International Wie Conference on Electrical and Computer Engineering (Wiecon-Ece)*, 2015, pp. 552–555.
71 J. A. Kolde and B. Bahar, *presented in part at the Proceedings of the First International Symposium on Proton Conducting Membrane Fuel Cells I*, Electrochemical Society Proceedings, Pennington, NJ, 1995.
72 J. Wang, X. Wang, P. Dou, H. Zhang and Y. Zhang, *Polym. Eng. Sci.*, 2015, **55**, 180–189.
73 S. M. J. Zaidi and T. Matsuura, *Polymer Membranes for Fuel Cells*, Springer, New York, 2009.
74 E. E. Abdel-Hady, M. O. Abdel-Hamed, S. Awad and M. F. M. Hmamm, *Polym. Adv. Technol.*, 2018, **29**, 130–142.
75 J. M. Bae, I. Honma, M. Murata, T. Yamamoto, M. Rikukawa and N. Ogata, *Solid State Ionics*, 2002, **147**, 189–194.
76 H. Diao, F. Yan, L. Qiu, J. Lu, X. Lu, B. Lin, Q. Li, S. Shang, W. Liu and J. Liu, *Macromolecules*, 2010, **43**, 6398–6405.
77 Y. He, J. Wang, H. Zhang, T. Zhang, B. Zhang, S. Cao and J. Liu, *J. Mater. Chem. A*, 2014, **2**, 9548–9558.
78 M. A. Hickner, H. Ghassemi, Y. S. Kim, B. R. Einsla and J. E. McGrath, *Chem. Rev.*, 2004, **104**, 4587–4611.
79 P. Costamagna, C. Yang, A. B. Bocarsly and S. Srinivasan, *Electrochim. Acta*, 2002, **47**, 1023–1033.
80 W. Mabrouk, L. Ogier, C. Sollogoub, S. Vidal, F. Matoussi and J. F. Fauvarque, *Desalin. Water Treat.*, 2015, **56**, 2637–2645.
81 D. Zhao, J. Li, M.-K. Song, B. Yi, H. Zhang and M. Liu, *Adv. Energy Mater.*, 2011, **1**, 203–211.
82 C. Wang, Z. Feng, Y. Zhao, X. Li, W. Li, X. Xie, S. Wang and H. Hou, *Int. J. Hydrogen Energy*, 2017, **42**, 29988–29994.
83 J. Souquet-Grumey, R. Perrin, J. Cellier, J. Bigarré and P. Buvat, *J. Membr. Sci.*, 2014, **466**, 200–210.
84 J. Miyake, M. Kusakabe, A. Tsutsumida and K. Miyatake, *ACS Appl. Energy Mater.*, 2018, **1**, 1233–1238.
85 J. Miyake, R. Taki, T. Mochizuki, R. Shimizu, R. Akiyama, M. Uchida and K. Miyatake, *Sci. Adv.*, 2017, **3**, eaao0476.
86 C. del Río, E. Morales and P. G. Escribano, *Int. J. Hydrogen Energy*, 2014, **39**, 5326–5337.
87 C. Beauger, G. Lainé, A. Burr, A. Taguet and B. Otazaghine, *J. Membr. Sci.*, 2015, **495**, 392–403.
88 M.-Y. Lim and K. Kim, *Polymers*, 2018, **10**, 569.
89 X. Sun, S. C. Simonsen, T. Norby and A. Chatzitakis, *Membranes*, 2019, **9**, 83.
90 J. Wang, B. Li, T. Yersak, D. Yang, Q. Xiao, J. Zhang and C. Zhang, *J. Mater. Chem. A*, 2016, **4**, 11559–11581.
91 M. Kim and D. G. Lee, *J. Power Sources*, 2016, **315**, 86–95.
92 Y. H. Seo, H. J. Kim, W. K. Jang and B. H. Kim, *Int. J. Precis. Eng. Manuf.*, 2014, **1**, 101–106.
93 C. K. Poh, Z. Tian, N. Bussayajarn, Z. Tang, F. Su, S. H. Lim, Y. P. Feng, D. Chua and J. Lin, *J. Power Sources*, 2010, **195**, 8044–8051.
94 E. Navaei Alvar, B. Zhou and S. H. Eichhorn, *Int. J. Energy Res.*, 2017, **41**, 1626–1641.
95 W. Xia, A. Mahmood, Z. Liang, R. Zou and S. Guo, *Angew. Chem., Int. Ed. Engl.*, 2016, **55**, 2650–2676.
96 H. A. Gasteiger, S. S. Kocha, B. Sompalli and F. T. Wagner, *Appl. Catal., B*, 2005, **56**, 9–35.
97 X. X. Wang, S. Hwang, Y. T. Pan, K. Chen, Y. He, S. Karakalos, H. Zhang, J. S. Spendelow, D. Su and G. Wu, *Nano Lett.*, 2018, **18**, 4163–4171.
98 Z. W. Seh, J. Kibsgaard, C. F. Dickens, I. Chorkendorff, J. K. Norskov and T. F. Jaramillo, *Science*, 2017, **355**, eaad4998.
99 E. J. Coleman, M. H. Chowdhury and A. C. Co, *ACS Catal.*, 2015, **5**, 1245–1253.
100 D. Banham and S. Ye, *ACS Energy Lett.*, 2017, **2**, 629–638.
101 A. Ganesan and M. Narayanasamy, *Mater. Renew. Sustain. Energy*, 2019, **8**, 18.
102 B. Krishnamurthy and S. Deepalochani, *Int. J. Electrochem. Sci.*, 2009, **4**, 386–395.
103 K. Nagasawa, S. Takao, K. Higashi, S. Nagamatsu, G. Samjeske, Y. Imaizumi, O. Sekizawa, T. Yamamoto, T. Uruga and Y. Iwasawa, *Phys. Chem. Chem. Phys.*, 2014, **16**, 10075–10087.
104 S. C. Zignani, V. Baglio, D. Sebastian, A. Sacca, I. Gatto and A. S. Arico, *Materials*, 2017, **10**, ma10030317.
105 C. J. Tseng, S. T. Lo, S. C. Lo and P. P. Chu, *Mater. Chem. Phys.*, 2006, **100**, 385–390.
106 L. Chong, J. Wen, J. Kubal, F. G. Sen, J. Zou, J. Greeley, M. Chan, H. Barkholtz, W. Ding and D. J. Liu, *Science*, 2018, **362**, 1276–1281.
107 J. Y. Chen, B. Lim, E. P. Lee and Y. N. Xia, *Nano Today*, 2009, **4**, 81–95.
108 Z. Jiang, J. Yu, T. Huang and M. Sun, *Polymers*, 2018, **10**, E1397.

109 X. X. Yuan, X. L. Ding, C. Y. Wang and Z. F. Ma, *Energy Environ. Sci.*, 2013, **6**, 1105–1124.
110 A. P. Mártire, G. M. Segovia, O. Azzaroni, M. Rafti and W. Marmisollé, *Mol. Syst. Des. Eng.*, 2019, **4**, 893–900.
111 A. Steinbach, D. van der Vliet, A. Komlev, D. Miller, S. Luopa, A. Hester, J. Sieracki, M. Yandrasits and M. Pejsa, *V.C.1 High Performance, Durable, Low Cost Membrane Electrode Assemblies for Transportation Applications*, DOE Hydrogen and Fuel Cells, US, 2013.
112 T. Abdel-Baset, T. Benjamin, R. Borup, K. E. Martin, N. Garland, S. Hirano, J. Kopasz, B. Lakshmanan, D. Masten, M. Mehall, D. Myers, D. Papageorgopoulos, W. Podolski, W. Podolski, B. Vermeersch and J. Waldecker, *Fuel Cell Technical Team Roadmap*, U.S. Department of Energy, Fuel Cell Technologies Office, US, 2013.
113 H.-J. Zhang, X. Yuan, L. Sun, X. Zeng, Q.-Z. Jiang, Z. Shao and Z.-F. Ma, *Int. J. Hydrogen Energy*, 2010, **35**, 2900–2903.
114 J. Greeley, I. E. Stephens, A. S. Bondarenko, T. P. Johansson, H. A. Hansen, T. F. Jaramillo, J. Rossmeisl, I. Chorkendorff and J. K. Norskov, *Nat. Chem.*, 2009, **1**, 552–556.
115 H. Meng, D. Zeng and F. Xie, *Catalysts*, 2015, **5**, 1221–1274.
116 Z.-M. Zhou, Z.-G. Shao, X.-P. Qin, X.-G. Chen, Z.-D. Wei and B.-L. Yi, *Int. J. Hydrogen Energy*, 2010, **35**, 1719–1726.
117 W. Wang, Z. Wang, J. Wang, C. J. Zhong and C. J. Liu, *Adv. Sci.*, 2017, **4**, 1600486.
118 J. Liu, Y. Li, Z. Wu, M. Ruan, P. Song, L. Jiang, Y. Wang, G. Sun and W. Xu, *J. Phys. Chem. C*, 2018, **122**, 14691–14697.
119 Q. Zhang, I. Lee, J. B. Joo, F. Zaera and Y. Yin, *Acc. Chem. Res.*, 2013, **46**, 1816–1824.
120 R. Liu and R. D. Priestley, *J. Mater. Chem. A*, 2016, **4**, 6680–6692.
121 X. Liu, J. Du, Y. Shao, S. F. Zhao and K. F. Yao, *Sci. Rep.*, 2017, **7**, 10249.
122 X. Tian, J. Luo, H. Nan, H. Zou, R. Chen, T. Shu, X. Li, Y. Li, H. Song, S. Liao and R. R. Adzic, *J. Am. Chem. Soc.*, 2016, **138**, 1575–1583.
123 K. A. Kuttiyiel, Y. Choi, S.-M. Hwang, G.-G. Park, T.-H. Yang, D. Su, K. Sasaki, P. Liu and R. R. Adzic, *Nano Energy*, 2015, **13**, 442–449.
124 P. Mani, R. Srivastava and P. Strasser, *J. Phys. Chem. C*, 2008, **112**, 2770–2778.
125 Y. Bing, H. Liu, L. Zhang, D. Ghosh and J. Zhang, *Chem. Soc. Rev.*, 2010, **39**, 2184–2202.
126 B. Lim, M. Jiang, P. H. Camargo, E. C. Cho, J. Tao, X. Lu, Y. Zhu and Y. Xia, *Science*, 2009, **324**, 1302–1305.
127 Z. Chen, M. Waje, W. Li and Y. Yan, *Angew. Chem., Int. Ed. Engl.*, 2007, **46**, 4060–4063.
128 Y.-W. Lee, S. Cha, K.-W. Park, J. I. Sohn and J. M. Kim, *J. Nanomater.*, 2015, **2015**, 1–20.
129 C. Chen, Y. Kang, Z. Huo, Z. Zhu, W. Huang, H. L. Xin, J. D. Snyder, D. Li, J. A. Herron, M. Mavrikakis, M. Chi, K. L. More, Y. Li, N. M. Markovic, G. A. Somorjai, P. Yang and V. R. Stamenkovic, *Science*, 2014, **343**, 1339–1343.
130 Y.-J. Wang, W. Long, L. Wang, R. Yuan, A. Ignaszak, B. Fang and D. P. Wilkinson, *Energy Environ. Sci.*, 2018, **11**, 258–275.
131 D. Dixon, J. Melke, M. Botros, J. Rathore, H. Ehrenberg and C. Roth, *Int. J. Hydrogen Energy*, 2013, **38**, 13393–13398.
132 M. D. Maciá, J. M. Campiña, E. Herrero and J. M. Feliu, *J. Electroanal. Chem.*, 2004, **564**, 141–150.
133 J. Qian, M. Shen, S. Zhou, C.-T. Lee, M. Zhao, Z. Lyu, Z. D. Hood, M. Vara, K. D. Gilroy, K. Wang and Y. Xia, *Mater. Today*, 2018, **21**, 834–844.
134 Y. Kang, P. Yang, N. M. Markovic and V. R. Stamenkovic, *Nano Today*, 2016, **11**, 587–600.
135 Z. Duan and G. Wang, *J. Phys. Chem. C*, 2013, **117**, 6284–6292.
136 M. Wang, X. Qin, K. Jiang, Y. Dong, M. Shao and W.-B. Cai, *J. Phys. Chem. C*, 2017, **121**, 3416–3423.
137 J. Jiang, H. Gao, S. Lu, X. Zhang, C.-Y. Wang, W.-K. Wang and H.-Q. Yu, *J. Mater. Chem. A*, 2017, **5**, 9233–9240.
138 M. H. Shao, T. Huang, P. Liu, J. Zhang, K. Sasaki, M. B. Vukmirovic and R. R. Adzic, *Langmuir*, 2006, **22**, 10409–10415.
139 H. Zhang, M. S. Jin, Y. J. Xiong, B. Lim and Y. N. Xia, *Acc. Chem. Res.*, 2013, **46**, 1783–1794.
140 D. C. Higgins and Z. Chen, *Can. J. Chem. Eng.*, 2013, **91**, 1881–1895.
141 H. Lee, M. J. Kim, T. Lim, Y. E. Sung, H. J. Kim, H. N. Lee, O. J. Kwon and Y. H. Cho, *Sci. Rep.*, 2017, **7**, 5396.
142 A. Velázquez-Palenzuela, L. Zhang, L. Wang, P. L. Cabot, E. Brillas, K. Tsay and J. Zhang, *J. Phys. Chem. C*, 2011, **115**, 12929–12940.
143 U. I. Kramm, I. Herrmann-Geppert, J. Behrends, K. Lips, S. Fiechter and P. Bogdanoff, *J. Am. Chem. Soc.*, 2016, **138**, 635–640.
144 V. Costa Bassetto, J. Xiao, E. Oveisi, V. Amstutz, B. Liu, H. H. Girault and A. Lesch, *Appl. Catal.*, 2018, **563**, 9–17.
145 D. Banham, T. Kishimoto, T. Sato, Y. Kobayashi, K. Narizuka, J.-i. Ozaki, Y. Zhou, E. Marquez, K. Bai and S. Ye, *J. Power Sources*, 2017, **344**, 39–45.
146 D. Banham, T. Kishimoto, Y. Zhou, T. Sato, K. Bai, J. I. Ozaki, Y. Imashiro and S. Ye, *Sci. Adv.*, 2018, **4**, eaar7180.
147 Y. Imashiro, T. Kishimoto, T. Sato, J.-I. Ozaki and T. M. S. Kusadokoro, *US Pat.*, 20170194653A1, 2017.
148 M. Chisaka, Y. Ando, Y. Yamamoto and N. Itagaki, *Electrochim. Acta*, 2016, **214**, 165–172.
149 L. Lu, H. Xu, J. Shi, S. Zhu, H. Zhao and G. Wang, *J. Appl. Electrochem.*, 2018, **48**, 801–810.
150 W. Zheng, L. Wang, F. Deng, S. A. Giles, A. K. Prasad, S. G. Advani, Y. Yan and D. G. Vlachos, *Nat. Commun.*, 2017, **8**, 418.
151 J. Zhang, Z. Xia and L. Dai, *Sci. Adv.*, 2015, **1**, e1500564.
152 H. R. Colón-Mercado and J. B. Gaillard, *V.F.13 PGM Free Catalysts for PEMFC*, DOE Hydrogen and Fuel Cells Program, Annual Progress Report, 2015.
153 S. Samad, K. S. Loh, W. Y. Wong, T. K. Lee, J. Sunarso, S. T. Chong and W. R. Wan Daud, *Int. J. Hydrogen Energy*, 2018, **43**, 7823–7854.
154 M.-Q. Wang, W.-H. Yang, H.-H. Wang, C. Chen, Z.-Y. Zhou and S.-G. Sun, *ACS Catal.*, 2014, **4**, 3928–3936.
155 R. Bashyam and P. Zelenay, *Nature*, 2006, **443**, 63–66.

156 Y. Nabae, S. Nagata, T. Hayakawa, H. Niwa, Y. Harada, M. Oshima, A. Isoda, A. Matsunaga, K. Tanaka and T. Aoki, *Sci. Rep.*, 2016, **6**, 23276.
157 J. Shui, C. Chen, L. Grabstanowicz, D. Zhao and D. J. Liu, *Proc. Natl. Acad. Sci. U. S. A.*, 2015, **112**, 10629–10634.
158 Y. Nabae, Y. Kuang, M. Chokai, T. Ichihara, A. Isoda, T. Hayakawa and T. Aoki, *J. Mater. Chem. A*, 2014, **2**, 11561–11564.
159 Y. Li, Q. Li, H. Wang, L. Zhang, D. P. Wilkinson and J. Zhang, *Electrochem. Energy Rev.*, 2019, **2**, 518–538.
160 R. Ma, G. Lin, Y. Zhou, Q. Liu, T. Zhang, G. Shan, M. Yang and J. Wang, *npj Comput. Mater.*, 2019, **5**.
161 J. Hu, K. A. Kuttiyiel, K. Sasaki, C. Zhang and R. R. Adzic, *J. Electrochem. Soc.*, 2018, **165**, J3355–J3362.
162 H. A. Miller, A. Lavacchi, F. Vizza, M. Marelli, F. Di Benedetto, F. D'Acapito, Y. Paska, M. Page and D. R. Dekel, *Angew. Chem., Int. Ed. Engl.*, 2016, **55**, 6004–6007.
163 S. Kabir, K. Lemire, K. Artyushkova, A. Roy, M. Odgaard, D. Schlueter, A. Oshchepkov, A. Bonnefont, E. Savinova, D. C. Sabarirajan, P. Mandal, E. J. Crumlin, I. V. Zenyuk, P. Atanassov and A. Serov, *J. Mater. Chem. A*, 2017, **5**, 24433–24443.
164 J. Durst, C. Simon, F. Hasché and H. A. Gasteiger, *J. Electrochem. Soc.*, 2014, **162**, F190–F203.
165 P. Chandran, A. Ghosh and S. Ramaprabhu, *Sci. Rep.*, 2018, **8**, 3591.
166 A. Ghosh, P. Chandran and S. Ramaprabhu, *Appl. Energy*, 2017, **208**, 37–48.
167 E. You, M. Min, S.-A. Jin, T. Kim and C. Pak, *J. Electrochem. Soc.*, 2018, **165**, F3094–F3099.
168 F. Tzorbatzoglou, A. Brouzgou, S. Jing, Y. Wang, S. Song and P. Tsiakaras, *Int. J. Hydrogen Energy*, 2018, **43**, 11766–11777.
169 E. Antolini, *Energy Environ. Sci.*, 2009, **2**, 915–931.
170 P. Chandran and S. Ramaprabhu, *Int. J. Hydrogen Energy*, 2018, **43**, 18477–18487.
171 K. Kwon, S.-a. Jin, K. H. Lee, D. J. You and C. Pak, *Catal. Today*, 2014, **232**, 175–178.
172 K. Guo, K.-M. Shi, J.-W. Guo and X.-L. Xie, *Electrochim. Acta*, 2017, **229**, 183–196.
173 W. Ni, A. Krammer, C. S. Hsu, H. M. Chen, A. Schuler and X. Hu, *Angew. Chem., Int. Ed. Engl.*, 2019, **58**, 7445–7449.
174 C. M. Zalitis, A. R. Kucernak, J. Sharman and E. Wright, *J. Mater. Chem. A*, 2017, **5**, 23328–23338.
175 S. Gudmundsdottir, E. Skulason, K. J. Weststrate, L. Juurlink and H. Jonsson, *Phys. Chem. Chem. Phys.*, 2013, **15**, 6323–6332.
176 C. A. Campos-Roldán and N. Alonso-Vante, *Electrochem. Energy Rev.*, 2019, **2**, 312–331.
177 Y. J. Wang, D. P. Wilkinson and J. Zhang, *Chem. Rev.*, 2011, **111**, 7625–7651.
178 Y. Jeon, Y. Ji, Y. I. Cho, C. Lee, D. H. Park and Y. G. Shul, *ACS Nano*, 2018, **12**, 6819–6829.
179 R. Omrani and B. Shabani, *Energies*, 2019, **12**, en12050855.
180 S. M. Haile, *Acta Mater.*, 2003, **51**, 5981–6000.
181 J. Benziger, J. Nehlsen, D. Blackwell, T. Brennan and J. Itescu, *J. Membr. Sci.*, 2005, **261**, 98–106.
182 Y. M. Vol'fkovich, V. E. Sosenkin, N. F. Nikol'skaya and T. L. Kulova, *Russ. J. Electrochem.*, 2011, **44**, 278–285.
183 L. Giorgi, E. Antolini, A. Pozio and E. Passalacqua, *Electrochim. Acta*, 1998, **43**, 3675–3680.
184 D. L. Wood, C. Rulison and R. L. Borup, *J. Electrochem. Soc.*, 2010, **157**, B195–B206.
185 D. M. Fadzillah, M. I. Rosli, M. Z. M. Talib, S. K. Kamarudin and W. R. W. Daud, *Renewable Sustainable Energy Rev.*, 2017, **77**, 1001–1009.
186 A. D. Santamaria, P. K. Das, J. C. MacDonald and A. Z. Weber, *J. Electrochem. Soc.*, 2014, **161**, F1184–F1193.
187 M. Mortazavi and K. Tajiri, *Int. J. Hydrogen Energy*, 2014, **39**, 9409–9419.
188 E. F. Medici and J. S. Allen, *J. Power Sources*, 2009, **191**, 417–427.
189 P. K. Sinha and C.-Y. Wang, *Electrochim. Acta*, 2007, **52**, 7936–7945.
190 P. K. Das, A. D. Santamaria and A. Z. Weber, *Procedia Eng.*, 2015, **105**, 751–756.
191 K. Jiao and X. Li, *Int. J. Hydrogen Energy*, 2010, **35**, 9095–9103.
192 P. K. Das, A. Grippin, A. Kwong and A. Z. Weber, *J. Electrochem. Soc.*, 2012, **159**, B489–B496.
193 T. J. Ko, S. H. Kim, B. K. Hong, K. R. Lee, K. H. Oh and M. W. Moon, *ACS Appl. Mater. Interfaces*, 2015, **7**, 5506–5513.
194 E. E. Kimball, J. B. Benziger and Y. G. Kevrekidis, *Fuel Cells*, 2010, **10**, 530–544.
195 C. Simon, D. Kartouzian, D. Müller, F. Wilhelm and H. A. Gasteiger, *J. Electrochem. Soc.*, 2017, **164**, F1697–F1711.
196 A. Hermann, T. Chaudhuri and P. Spagnol, *Int. J. Hydrogen Energy*, 2005, **30**, 1297–1302.
197 S. Karimi, N. Fraser, B. Roberts and F. R. Foulkes, *Adv. Mater. Sci. Eng.*, 2012, **2012**, 1–22.
198 R. A. Antunes, M. C. L. Oliveira, G. Ett and V. Ett, *Int. J. Hydrogen Energy*, 2010, **35**, 3632–3647.
199 S. T. Myung, S. Sakurada, M. Kumagai and H. Yashiro, *Fuel Cells*, 2010, **10**, 545–555.
200 R. L. Borup and N. E. Vanderborgh, *MRS Proceedings*, 2011, **393**, 151–155.
201 J. Wu, X. Z. Yuan, J. J. Martin, H. Wang, J. Zhang, J. Shen, S. Wu and W. Merida, *J. Power Sources*, 2008, **184**, 104–119.
202 S. Shimpalee, V. Lilavivat, H. McCrabb, Y. Khunatorn, H. K. Lee, W. K. Lee and J. W. Weidner, *Int. J. Hydrogen Energy*, 2016, **41**, 13688–13696.
203 C. A. C. Sequeira and L. Amaral, *J. Fuel Cell Sci. Technol.*, 2014, **11**, 044001-3.
204 F. Jaouen, S. Haasl, W. v. d. Wijngaart, A. Lundblad, G. Lindbergh and G. Stemme, *J. Power Sources*, 2005, **144**, 113–121.
205 J. P. Kopasz and T. G. Benjamin, *2017 Bipolar Plate Workshop Summary Report*, Fuel Cell Technologies Office, U.S. Department of Energy, US, 2017.
206 Y. Wang and D. O. Northwood, *J. Power Sources*, 2007, **165**, 293–298.

207 R. A. Antunes, M. C. L. de Oliveira, G. Ett and V. Ett, *J. Power Sources*, 2011, **196**, 2945–2961.
208 R. Taherian, *J. Power Sources*, 2014, **265**, 370–390.
209 O. A. Alo, I. O. Otunniyi, H. Pienaar and S. E. Iyuke, *Procedia Manufacturing*, 2017, **7**, 395–401.
210 A. E. Marquardt, E. M. Breitung, T. Drayman-Weisser, G. Gates and R. J. Phaneuf, *Heritage Sci.*, 2015, **3**, 37.
211 S. Chung, D. Shin, M. Choun, J. Kim, S. Yang, M. Choi, J. W. Kim and J. Lee, *J. Power Sources*, 2018, **399**, 350–356.
212 T. Mennola, M. Noponen, T. Kallio, M. Mikkola and T. Hottinen, *J. Appl. Electrochem.*, 2004, **34**, 31–36.
213 S. G. Kandlikar, M. L. Garofalo and Z. Lu, *Fuel Cells*, 2011, **11**, 814–823.
214 H. Li, Y. Tang, Z. Wang, Z. Shi, S. Wu, D. Song, J. Zhang, K. Fatih, J. Zhang, H. Wang, Z. Liu, R. Abouatallah and A. Mazza, *J. Power Sources*, 2008, **178**, 103–117.
215 M. Ji and Z. Wei, *Energies*, 2009, **2**, 1057–1106.
216 A. Forner-Cuenca, J. Biesdorf, L. Gubler, P. M. Kristiansen, T. J. Schmidt and P. Boillat, *Adv. Mater.*, 2015, **27**, 6317–6322.
217 Z. Wang, Y. Zeng, S. Sun, Z. Shao and B. Yi, *Int. J. Hydrogen Energy*, 2017, **42**, 21922–21929.
218 S. Litster, C. R. Buie, T. Fabian, J. K. Eaton and J. G. Santiago, *J. Electrochem. Soc.*, 2007, **154**, B1049–B1058.
219 R. Pandey, H. Agarwal, R. Kumar, S. Parthasarathi and S. Bhat, *US Pat.*, 20170141416A1, 2017.
220 T. Fabian, R. O'Hayre, S. Litster, F. B. Prinz and J. G. Santiago, *J. Power Sources*, 2010, **195**, 3201–3206.
221 B. Chen, W. Ke, M. Luo, J. Wang, Z. Tu, M. Pan, H. Zhang, X. Liu and W. Liu, *Energy*, 2015, **91**, 799–806.
222 J. Chen, J. B. Siegel, A. G. Stefanopoulou and J. R. Waldecker, *Int. J. Hydrogen Energy*, 2013, **38**, 5092–5105.
223 B. Chen, Z. Tu and S. H. Chan, *Appl. Therm. Eng.*, 2018, **129**, 968–978.
224 B. Chen, Y. Cai, J. Shen, Z. Tu and S. H. Chan, *Appl. Therm. Eng.*, 2018, **132**, 80–86.
225 Q. Meyer, S. Ashton, O. Curnick, T. Reisch, P. Adcock, K. Ronaszegi, J. B. Robinson and D. J. L. Brett, *J. Power Sources*, 2014, **254**, 1–9.
226 A. Gomez, A. P. Sasmito and T. Shamim, *Energy Convers. Manage.*, 2015, **106**, 951–957.
227 Y.-F. Lin and Y.-S. Chen, *J. Power Sources*, 2017, **340**, 176–182.
228 Y. Yang, X. Zhang, L. Guo and H. Liu, *Int. J. Hydrogen Energy*, 2018, **43**, 1769–1780.
229 Y. Yang, X. Zhang, L. Guo and H. Liu, *Int. J. Hydrogen Energy*, 2017, **42**, 28578–28587.
230 D. Santarosa, D. Pinto, V. Silva, R. Silva and C. Rangel, *Int. J. Hydrogen Energy*, 2007, **32**, 4350–4357.
231 S.-S. Hsieh and C.-F. Huang, *Energy Convers. Manage.*, 2013, **76**, 971–979.
232 J. Fernández-Moreno, G. Guelbenzu, A. J. Martín, M. A. Folgado, P. Ferreira-Aparicio and A. M. Chaparro, *Appl. Energy*, 2013, **109**, 60–66.
233 S. Kim, H. Cha, C. Miesse, J. Jang, Y. Oh and S. Cha, *Int. J. Hydrogen Energy*, 2009, **34**, 459–466.
234 A. Faghri and Z. Guo, *US Pat.*, 20060286436A1, 2006.
235 H.-A. Liu, S.-Y. Hu, Yu and C.-Y. Yu, *US Pat.*, 20060019129A1, 2006.
236 S. S. Giddey, F. T. Ciacchi and S. P. S. Badwal, *US Pat.*, 2008019975A1, 2008.
237 Y.-c. Eun, J.-h. Sauk, S.-j. An, G.-t. Roh and S.-r. Chang, *US Pat.*, 20080280183A1, 2008.
238 S. Mogi and M. Shibata, *US Pat.*, 2010068583A1, 2010.
239 S.-Y. Hu, H.-A. Liu, C.-Y. Yu, *US Pat.*, 20060121331A1, 2006.
240 S.-Y. Hu, H.-A. Liu, C.-Y. Yu, *US Pat.*, 008012642B2, 2011.
241 U. Basuli, J. Jose, R. H. Lee, Y. H. Yoo, K. U. Jeong, J. H. Ahn and C. Nah, *J. Nanosci. Nanotechnol.*, 2012, **12**, 7641–7657.
242 M. B. Sassin, Y. Garsany, B. D. Gould and K. E. Swider-Lyons, *Anal. Chem.*, 2017, **89**, 511–518.
243 S. Y. Cha and W. M. Lee, *J. Electrochem. Soc.*, 1999, **146**, 4055–4060.
244 S. Towne, V. Viswanathan, J. Holbery and P. Rieke, *J. Power Sources*, 2007, **171**, 575–584.
245 A. Ostroverkha, M. Dubaua, V. Johaneka, P. Kusa, I. Khalakhan, M. Vaclavua, R. Fialab, Y. Ostroverkha and V. Matolin, *ECS Trans.*, 2017, **80**(8), 839–845.
246 S. Shukla, K. Domican, K. Karan, S. Bhattacharjee and M. Secanell, *Electrochim. Acta*, 2015, **156**, 289–300.
247 L. I. Şanlı, B. Yarar, V. Bayram and S. A. Gürsel, *J. Mater. Sci.*, 2016, **52**, 2091–2102.
248 N. Chingthamai, K. Sombatmankhong and Y. Laoonual, *Energy Procedia*, 2017, **105**, 1806–1812.
249 A. M. Chaparro, M. A. Folgado, P. Ferreira-Aparicio, A. J. Martin, I. Alonso-Alvarez and L. Daza, *J. Electrochem. Soc.*, 2010, **157**, B993–B999.
250 X. Peng, T. Omasta, W. Rigdon and W. E. Mustain, *J. Electrochem. Soc.*, 2016, **163**, E407–E413.
251 A. M. Chaparro, P. Ferreira-Aparicio, M. A. Folgado, A. J. Martín and L. Daza, *J. Power Sources*, 2011, **196**, 4200–4208.
252 S. Litster and G. McLean, *J. Power Sources*, 2004, **130**, 61–76.
253 M. Lopez-Haro, L. Guetaz, T. Printemps, A. Morin, S. Escribano, P. H. Jouneau, P. Bayle-Guillemaud, F. Chandezon and G. Gebel, *Nat. Commun.*, 2014, **5**, 5229.
254 A. M. Chaparro, B. Gallardo, M. A. Folgado, A. J. Martín and L. Daza, *Catal. Today*, 2009, **143**, 237–241.
255 M. S. Çögenli, S. Mukerjee and A. B. Yurtcan, *Fuel Cells*, 2015, **15**, 288–297.
256 D. Gruber, N. Ponath, J. Müller and F. Lindstaedt, *J. Power Sources*, 2005, **150**, 67–72.
257 A. Ostroverkh, V. Johánek, M. Dubau, P. Kúš, I. Khalakhan, B. Šmíd, R. Fiala, M. Václavů, Y. Ostroverkh and V. Matolín, *Int. J. Hydrogen Energy*, 2019, **44**, 19344–19356.
258 M. Inaba, T. Suzuki, T. Hatanaka and Y. Morimoto, *J. Electrochem. Soc.*, 2015, **162**, F634–F638.
259 C.-T. Hsieh, Y.-Y. Liu, D.-Y. Tzou and W.-Y. Chen, *J. Phys. Chem. C*, 2012, **116**, 26735–26743.
260 H. Qayyum, C.-J. Tseng, T.-W. Huang and S.-y. Chen, *Catalysts*, 2016, **6**, 180.
261 E. H. Majlan, D. Rohendi, W. R. W. Daud, T. Husaini and M. A. Haque, *Renewable Sustainable Energy Rev.*, 2018, **89**, 117–134.
262 M. V. Williams, E. Begg, L. Bonville, H. R. Kunz and J. M. Fenton, *J. Electrochem. Soc.*, 2004, **151**, A1173–A1180.

263 M. Vatanatham, L. B. Y. Song, J. F. H. R. Kunz, A. Smirnova and X. Wang, *201st Electrochemical Society Meeting*, Philadelphia, PA, 2002.
264 M. V. Williams, L. E. K. Begg, J. Bonville, H. R. Kunz and J. M. Fenton, *ECS 202nd Meeting*, Salt Lake City, 2002.
265 E.-S. Lee, K.-H. Yang, H.-R. Jung,T.-H. Kim, S.-K. Han, J.-K. Lee, Y.-H. Seo and J.-H. Park, *US Pat.*, 20090011308A1, 2009.
266 X. Wang, H. Zhang, J. Zhang, H. Xu, X. Zhu, J. Chen and B. Yi, *J. Power Sources*, 2006, **162**, 474–479.
267 Y. Okuyama, S. Kuwata and K. Kodama, *US Pat.*, 9793550B2, 2012.
268 G.-G. Park, Y.-J. Sohn, T.-H. Yang, Y.-G. Yoon, W.-Y. Lee and C.-S. Kim, *J. Power Sources*, 2004, **131**, 182–187.
269 J. F. Lin, J. Wertz, R. Ahmad, M. Thommes and A. M. Kannan, *Electrochim. Acta*, 2010, **55**, 2746–2751.
270 J. R. Yu, Y. Yoshikawa, T. Matsuura, M. N. Islam and M. Hori, *Electrochem. Solid-State Lett.*, 2005, **8**, A152–A155.
271 H.-K. Lee, J.-H. Park, D.-Y. Kim and T.-H. Lee, *J. Power Sources*, 2004, **131**, 200–206.
272 V. Yarlagadda, S. E. McKinney, C. L. Keary, L. Thompson, B. Zulevi and A. Kongkanand, *J. Electrochem. Soc.*, 2017, **164**, F845–F849.
273 H. Abaoud, M. Ghouse, K. Lovell and G. Almotairy, *Int. J. Hydrogen Energy*, 2005, **30**, 385–391.
274 A. M. Kannan, S. Sadananda, D. Parker, L. Munukutla, J. Wertz and M. Thommes, *J. Power Sources*, 2008, **178**, 231–237.
275 C. Lim and C. Y. Wang, *Electrochim. Acta*, 2004, **49**, 4149–4156.
276 L. Cindrella, A. M. Kannan, J. F. Lin, K. Saminathan, Y. Ho, C. W. Lin and J. Wertz, *J. Power Sources*, 2009, **194**, 146–160.
277 L.-Y. Meng and S.-J. Park, *Carbon letters*, 2014, **15**, 89–104.
278 P. Shrestha, R. Banerjee, J. Lee, N. Ge, D. Muirhead, H. Liu, A. K. C. Wong, D. Ouellette, B. Zhao and A. Bazylak, *J. Power Sources*, 2018, **402**, 468–482.
279 H.-F. Lee, J.-Y. Chang and Y. W. Chen-Yang, *RSC Adv.*, 2018, **8**, 22506–22514.
280 M. Tomas, I. S. Biswas, P. Gazdzicki, L. Kullova and M. Schulze, *Mater. Renew. Sustain. Energy*, 2017, **6**.
281 E. Middelman, W. Kout, B. Vogelaar, J. Lenssen and E. de Waal, *J. Power Sources*, 2003, **118**, 44–46.
282 M. S. Wilson and D. N. Busick, *US Pat.*, 6248467B1, 2001.
283 B. K. Kakati and D. Deka, *Electrochim. Acta*, 2007, **52**, 7330–7336.
284 R. Taherian, A. N. Golikand and M. J. Hadianfard, *Mater. Des.*, 2011, **32**, 3883–3892.
285 M. Belali-Owsia, M. Bakhshi-Jooybari, S. J. Hosseinipour and A. H. Gorji, *Int. J. Adv. Manuf. Technol.*, 2014, **77**, 1281–1293.
286 H. Kahraman, I. Cevik, F. Dündar and F. Ficici, *Arabian J. Sci. Eng.*, 2016, **41**, 1961–1968.
287 D. Zhang, L. Duan, L. Guo, Z. Wang, J. Zhao, W.-H. Tuan and K. Niihara, *Int. J. Hydrogen Energy*, 2011, **36**, 9155–9161.
288 N. F. Asri, T. Husaini, A. B. Sulong, E. H. Majlan and W. R. W. Daud, *Int. J. Hydrogen Energy*, 2017, **42**, 9135–9148.
289 H. Zhang, G. Lin, M. Hou, L. Hu, Z. Han, Y. Fu, Z. Shao and B. Yi, *J. Power Sources*, 2012, **198**, 176–181.
290 M. Dinu, E. Mouele, A. Parau, A. Vladescu, L. Petrik and M. Braic, *Coatings*, 2018, **8**, 132.
291 M. Elyasi, H. T. Ghadikolaee and M. Hosseinzadeh, *Int. J. Adv. Manuf. Technol.*, 2017, **92**, 765–776.
292 M. Wu, C. Lu and D. Wen, *Mater. Res. Innovations*, 2015, **19**, S-85–S-88.
293 X. Li and I. Sabir, *Int. J. Hydrogen Energy*, 2005, **30**, 359–371.
294 S. S. Hsieh, C. F. Huang and C. L. Feng, *Micron*, 2008, **39**, 263–268.
295 R. Hahn, S. Wagner, A. Schmitz and H. Reichl, *J. Power Sources*, 2004, **131**, 73–78.
296 T. Wang, J. Zhang, D. Zheng, C. Chen, X. Xinxin Li, C. Yang and B. Xi, *Open Fuels Energy Sci. J.*, 2008, **1**, 46–50.
297 X. G. Zhang, T. Wang, D. Zheng, J. Zhang, Y. Zhang, L. Zhu, C. Chen, J. Yan, H. H. Liu, Y. W. Lou, X. X. Li and B. J. Xia, *Int. J. Electrochem. Sci.*, 2007, **2**, 618–626.
298 R. J. Dawson, A. J. Patel, A. E. W. Rennie and S. White, *J. Appl. Electrochem.*, 2015, **45**, 637–645.
299 M. Filipowicz, P. Dudek, A. Raźniak, B. Lis, M. Dudek, T. Olkuski and K. Styszko, *E3S Web Conf.*, 2016, **10**, 00127.
300 A. Zhakeyev, P. Wang, L. Zhang, W. Shu, H. Wang and J. Xuan, *Adv. Sci.*, 2017, **4**, 1700187.
301 V. Jayakumar, A. Jayakumar, S. Ranganathan, D. Devika and S. Sridevi, *MATEC Web Conf.*, 2018, **172**, 04005.
302 K. V. Wong and A. Hernandez, *ISRN Mech. Eng.*, 2012, **2012**, 1–10.
303 Y. Wang, L. Pham, G. P. S. d. Vasconcellos and M. Madou, *J. Power Sources*, 2010, **195**, 4796–4803.
304 T. Pichonat and B. Gauthier-Manuel, *Dtip 2006: Symposium on Design, Test, Integration and Packaging of Mems/Moems 2006*, 2006.
305 S. A. M. Tofail, E. P. Koumoulos, A. Bandyopadhyay, S. Bose, L. O'Donoghue and C. Charitidis, *Mater. Today*, 2018, **21**, 22–37.
306 A. Kongkanand, N. P. Subramanian, Y. Yu, Z. Liu, H. Igarashi and D. A. Muller, *ACS Catal.*, 2016, **6**, 1578–1583.
307 T. Yang, P. Shi and C. Du, *Electrochim. Acta*, 2006, **51**, 5618–5625.
308 T. Yang and P. Shi, *Int. J. Hydrogen Energy*, 2008, **33**, 2795–2801.
309 A. Schmitz, C. Ziegler, J. O. Schumacher, M. Tranitz, E. Fontes and C. Hebling, *Fuel Cells*, 2004, **4**, 358–364.
310 S. H. Kim, C. M. Miesse, H. B. Lee, I. W. Chang, Y. S. Hwang, J. H. Jang and S. W. Cha, *Appl. Energy*, 2014, **134**, 382–391.
311 A. Strong, C. Thornberry, S. Beattie, R. Chen and S. R. Coles, *J. Fuel Cell Sci. Technol.*, 2015, **12**(6), 064001.
312 M. S. Wilson and S. Gottesfeld, *J. Electrochem. Soc.*, 1992, **139**, L28–L30.
313 X. Ding, S. Didari, T. F. Fuller and T. A. L. Harris, *J. Electrochem. Soc.*, 2012, **159**, B746–B753.
314 T. Nakakubo, M. Shibata and K. Yasuda, *J. Electrochem. Soc.*, 2005, **152**, A2316–A2322.
315 S. H. Akella, D. Ebenzer, S. R. Sai Siddhardha, A. Ahire and N. K. Mal, *Sci. Rep.*, 2018, **8**, 12082.

